

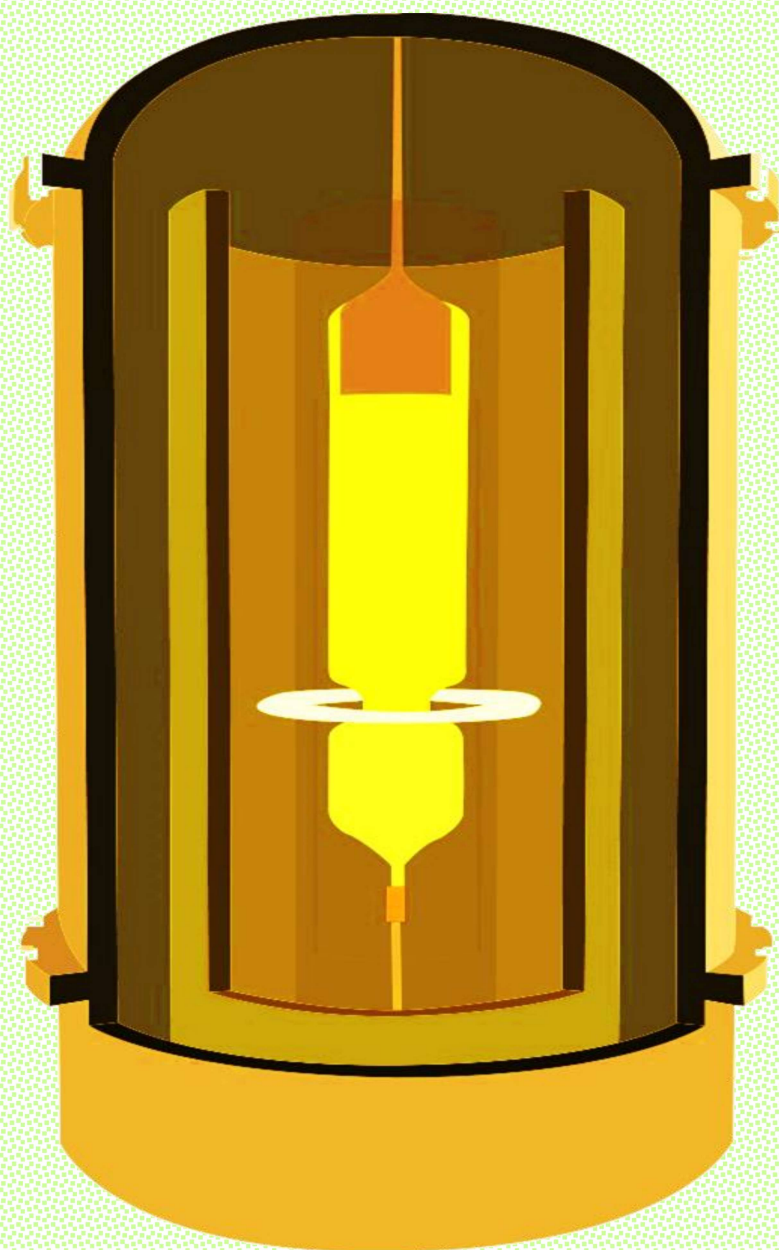


e-ISSN: 3048-460X

CNS&E

Current Natural
Sciences &
Engineering

Peer-reviewed, Multidisciplinary Journal



High Quality
Silicon Single
Crystal Puller
by Czochralski
Technique is
Foundation for
Microprocessor,
Solar Cell &
Most of
Electronics
Devices !

<http://doi.org/10.63015/cnse-2025.2.3>

Volume 2 Issue 3, July 2025

About CNS&E

Current Natural Sciences & Engineering (CNS&E) Journal publishes new, innovative and cutting-edge research in Natural sciences including physical, chemical, biological, agricultural and environmental sciences, metrology, and other related interdisciplinary fields. Scientific research results in the form of high-quality manuscripts, review articles, mini-reviews, reports, news and short communications are highly welcome.

CNS&E is a hybrid, bimonthly, multidisciplinary journal published by the Vigyanvardhan Blessed Foundation (VBF), a non-profit organization working to disseminate science for the betterment of society.

Scope: CNS&E journal has a broad multidimensional scope. It publishes research in the areas of:

- ☐ Hydrogen & Renewable Energy
- ☐ Environmental Sciences & Hydroelectric Cell
- ☐ Artificial Intelligence Convergence in S&T
- ☐ Net Carbon Zero & Earth Sustainability
- ☐ Condensed Matter & Nanomaterials
- ☐ Health Science & Technology
- ☐ Nuclear Science: Health & Society
- ☐ Measurement Science & Industrial Research
- ☐ Digital & Sustainable Agriculture
- ☐ Smart Engineering Materials & Sensors

Publication Policy: The journal maintains integrity and high ethical values. Submitted manuscripts are peer-reviewed and evaluated for novel scientific content irrespective of its origin. The information about a submitted manuscript will be confidential and will not be disclosed other than Chief Editor, editorial staff, corresponding author, reviewers, and the publisher. The journal ensures that any unpublished work must not be used in Editor's, and reviewer's own research without the explicit written consent of the author(s).

Publication Decisions: The Chief Editor of the journal is responsible for deciding the publication or rejection of the submitted manuscript. The Chief Editor may take suggestion with other editors or reviewers in making decision.

Publisher: VB Foundation

CNS&E Editorial Board

Chief Editor

Prof. (Dr.) R K Kotnala,

Former Chairman NABL, Raja Ramanna Fellow DAE &
Chief Scientist, CSIR-National Physical Laboratory

Senior Editors

Prof. A C Pandey

Director, Inter University Accelerator
Centre, New Delhi, India

Prof. K K Pant

Director IIT Roorkee, Uttarakhand, India

Prof. R K Sinha

Department of Applied Physics, DTU
Former Vice Chancellor, Gautam Buddha
University and CSIR-CSIO Chandigarh

Prof Sanjay Sharma

Director Indian Culture Study Centre-GBU
School of Information and Communication
Technology Gautam Buddha University,
Greater Noida (UP)

Prof. Bhanooduth Lalljee,

President, Sustainable Agricultural
Organisation, External Professor at the
Mauritius Institute of Education (MIE) and
JSS Academy, Mauritius.

Editors

Dr. Indra Mani

Vice-Chancellor, Vasantrya Naik
Marathwada Krishi Vidyapeeth,
Maharashtra, India

Prof Nitin Puri

Executive Director-NIELIT, Patna Bihar
Professor-Delhi Technological University,
Delhi

Prof Ajay Dhar

Associate Director, Academy of Scientific
and Innovative Research, AcSIR,
Ghaziabad-UP, India

Dr D S Rawal

Outstanding Scientist (Scientist-H) Solid
State Physics Laboratory (SSPL), DRDO,
Lucknow Road, Delhi

Prof Ambesh Dixit

Department of Physics, Indian Institute of
Technology, Jodhpur, Rajasthan

Prof Deepak Pant

Department of Chemistry and
Environmental Sciences Dean, School of
Earth and Environmental Sciences; Head,
Department of Environmental Science
Central University of Himachal Pradesh.

Prof Manoranjan Kar

Department of Physics, Indian Institute of
Technology, Patna, Bihar

Dr A K Srivastava

Former Director, CSIR-Advanced
Materials and Processes Research Institute,
CSIR-AMPRI, Bhopal

Dr. S K Jha

Former Outstanding Scientist and Head,
Radiation Protection Section (Nuclear
Fuels) Health Physics Division &
Professor, HBNI, Bhabha Atomic
Research Centre, Mumbai.

Dr. Nasimuddin

Principal Scientist, Antenna and Optical
Department, Institute for Infocomm
Research; Agency for Science,
Technology, and Research, Singapore.

Associate Editors

Prof. Kedar Singh

Professor & Dean of School of Physical Sciences, Jawaharlal Nehru University, New Delhi, India

Prof Satish Khasa

Professor & Former Director
Deenbandhu Chhotu Ram University of Science & Technology, Sonapat, Haryana

Dr. Rakesh Kr Singh

Academic Head, Aryabhatta Center for Nano Science and Nano Technology, Aryabhatta Knowledge University, Patna, India

Prof. Kamlesh Patel

Department of Electronic Science
University of Delhi South Campus Benito Juarez Road, New Delhi.

Dr. Anurag Gaur

Associate Prof- Department of Physics
Netaji Subhas University of Technology, New Delhi

Dr Jyoti Shah

Director-New Science Creators Institute,
Former DST-WoSA, CSIR-National Physical Laboratory, India

CNS&E Volume 2, Issue 3, July 2025

Table of contents:

S. No.	Title and Author	Page No.
1.	<i>Chief Editor's Message</i> Editorial Prof R K Kotnala	657-659
2.	Brief Overview of Seed Rotation Technique (SRT) Apparatus: An Effective Tool for Growing Bulk Size Single Crystals Kiran, N. Vijayan, Jyoti, Chetan	660-667
3.	Study of p-GaN Gate HEMT's Structural and Geometrical Parameters to Realise E-mode HEMT for 750V Switch Operation Sonalee Kapoor, Khuswant Sehra, Niraj Kumar and D S Rawal	668-673
4.	Classification and Analysis of 12-Lead Electrocardiograms Revanth Reddy Pasula	674-681
5.	Advancements in CPW-Fed Antennas: Design Techniques and Performance Optimization for 5G and Beyond Manish Kumar, Sandeep Kumar Singh, Arvind Kumar Singh, Tripurari Sharan	682-704
6.	The Impact of Stress on Education: Understanding the Consequences and Finding Solutions (News & Views) Rooma Pathak	705-707

Chief Editor's Message

Editorial

Prof R K Kotnala

FNASC, FIGU, FMSI

Chief Editor, Current Natural Sciences & Engineering, Journal (CNS&E)

DOI: <https://doi.org/10.63015/kotnala.2025.2.3>

Email: rkkotnala@gmail.com

I feel highly privileged to address the preface of the ninth issue of an esteemed journal the Current Natural Science & Engineering (CNS&E), which has gained an overwhelming popularity within a short time. It is well known that today India ranks first in Engineering Institutions infrastructure in the world. To fulfil such a huge demand to quickly publish high quality research papers within 40 days, hence this journal is serving the purpose of a comprehensive interdisciplinary integrated journal at global level to serve the scientific community in a better way. The CNSE is providing a unique platform worldwide to publish new findings of Scientists, Researchers & Engineers involved in the new science creation, research, innovative design, and development for industries in the benefit of the society.

The Current Natural Science & Engineering Journal (CNS&E) is an excellent forum to convey the innovative research findings, latest breakthrough inventions, discoveries, and future research prospects in new science for the welfare of society. Scholarly articles published in peer reviewed CNS&E reveals a well known fact that journal supports scientific fraternity worldwide by providing them with novel innovations/improvements by facilitating the proper directions for additional research, inventions, discoveries. Besides, it also rapidly provides an opportunity to discuss incredibly relevant scientific questions arising from continuously proceeding research areas and, hence, nucleates origin for more reliable and insightful answers to mind-boggling inquisitiveness of researchers.

The CNS&E international journal publishes the finest, cutting edge, Industrial processes and application-oriented peer-reviewed research in the fields of Physical & Engineering Sciences, AI & Computer Science, Energy, Metrology and Standardization, Chemical Sciences, Nuclear and Environmental Sciences, Health Science and Digital Agriculture purely on the basis of scientific validity, novelty with high ethical standards.

The present issue enumerates very critical studies on single crystals emerging in advanced technology effectively owing to their superior physical, optical and electronic properties as they serve as fundamental building blocks in advancing various domains, including optoelectronics, nonlinear optics, laser technology and photonics. The presented work portrays an overview on the seed rotation technique (SRT) description and explores the impact of several parameters on crystal quality, as well as the mechanisms that contribute to defect reduction and enhanced structural integrity. In the present article, it provides a brief discussion on the seed rotation technique used in solution-based crystal growth methods to enhance the size and quality of crystals. It promotes convective mixing within the solution, hence reducing localized temperature variations and facilitating a more uniform thermal environment for the developing crystal. The enhanced thermal

uniformity can indirectly mitigate the negative consequences usually linked to abrupt heat gradients, including strain and fault formation during growth. Rotation also facilitates enhanced crystal symmetry and homogeneity, which are crucial for the performance and reliability of crystals utilized in semiconductor, optical and advanced material applications.

A very important application of E-mode GaN HEMTs have been reported on the preferred device configuration for the use in high power switching applications on p-GaN gate HEMT structure and device geometry to achieve high breakdown voltage for DC to DC power switching applications. Various HEMT device geometrical parameters have been explored as a function of device electrical parameters such as Drain current, threshold voltage R_{on} and breakdown voltage. The gate -drain spacing of greater than 10 μm is found to be the most critical dimension for achieving high breakdown voltage ~ 750 V but at the cost of device current handling capability which is found to be decreasing from 960 mA/mm to 900 mA/mm when gate drain spacing of 6 μm is increased to 10 μm .

In Biomedical application the present study investigates the classification of 12-lead electrocardiogram (ECGs) to detect abnormalities in the heart using three computational techniques. It has been mainly focussed on (1) gradient-boosted ensembling following manual feature extraction, (2) deep learning with stacked autoencoders connected to the output of a multi-layer perceptron (MLP) classifier, and (3) a fusion model combining deep-learning and manually extracted features based on an experiment, which has been conducted using the PhysioNet/Computing in Cardiology Challenge 2020 database, addressing a multi-level classification task involving 27 heartbeat rhythm diagnoses. The best-performing model, merged with handcrafted features with autoencoder-derived features, achieves an average classification accuracy of 30.7% and a challenge metric score of 0.4366.

A comprehensive review explores recent advancements in coplanar waveguide (CPW)-fed antenna design, with a particular focus on performance optimization techniques applicable to 5G and future 6G wireless systems. It provides a roadmap for selecting optimal design combinations tailored to specific wireless standards and platforms. Future research is encouraged to explore reconfigurable structures, AI-driven design automation, transparent and sustainable materials, and energy-harvesting integration for next-generation intelligent antenna systems. The study investigates a wide array of design methodologies including the integration of stubs, slots, strips, corner truncation, substrate engineering, defected ground structures (DGS), defected substrates, metamaterials (MTM), frequency-selective surfaces (FSS), conductor-backed (CB) configurations, modified ground structures (MGS), metal reflectors, and MIMO architectures. A detailed parametric comparison reveals how these approaches significantly enhance key antenna parameters such as impedance bandwidth (up to 181%), gain (up to 13.1 dBi), axial ratio bandwidth, miniaturization (up to 72.7% size reduction), polarization purity, and frequency agility across multiple bands. Applications span 5G/6G mobile, biomedical, IoT, satellite, CubeSat, and vehicular systems. In particular, techniques like MIMO and metamaterial integration deliver high port isolation (≥ 15 dB), ultra-wideband (UWB) support, and enhanced diversity performance.

News & Views on the Impact of Stress on Education is a guiding factor for the students : Understanding the Consequences and Finding Solutions Stress and education are intricately linked, with the pressure to perform well academically often taking a toll on students' mental and emotional well-being. Chronic stress can have severe consequences on students' cognitive,

emotional, and social development, ultimately affecting their academic achievement and overall quality of life.

Current Natural Sciences & Engineering (CNS&E) Journal with Global Visibility & Reach has redefined the publication journey. The Scholars groundbreaking research and innovative ideas no longer face unnecessary delays/snags/biasing. Our streamlined review and editing system ensures that innovative work swiftly reaches the global academic community, gaining the recognition it truly deserves.

Swift Recognition at Global Level of the CNS&E Papers: Accelerated Publication Methodology Adopted to publish manuscript within 40 days in general ! Moreover, Scholars and institutions worldwide can easily locate, cite, and share your valuable research published in CNS&E journal.

To further widening the scope of the journal, a distinguished team of renowned editors has been further reinforced by the following nine distinct highly specialised experts as editors:

Prof Sanjay Sharma

Director Indian Culture Study Centre-GBU
School of Information and Communication
Technology Gautam Buddha University,
Greater Noida (UP)

Prof Nitin Puri

Executive Director-NIELIT, Patna Bihar
Professor-Delhi Technological University,
Delhi

Dr D S Rawal

Outstanding Scientist (Scientist-H)
Solid State Physics Laboratory (SSPL),
DRDO, Lucknow Road, Delhi

Prof Ambesh Dixit

Department of Physics
Indian Institute of Technology, Jodhpur,
Rajasthan

Prof Deepak Pant

Department of Chemistry and Environmental
Sciences Dean, School of Earth and

Environmental Sciences; Head, Department
of Environmental Science Central University
of Himachal Pradesh, Himachal Pradesh -
India

Prof Manoranjan Kar

Department of Physics
Indian Institute of Technology, Patna, Bihar

Prof Satish Khosa

Professor & Former Director
Deenbandhu Chhotu Ram University of
Science & Technology, Sonapat, Haryana

Prof. Kamlesh Patel

Department of Electronic Science
University of Delhi South Campus Benito
Juarez Road, New Delhi.

Dr. Anurag Gaur

Associate Prof- Department of Physics
Netaji Subhas University of Technology,
New Delhi



Brief Overview of Seed Rotation Technique (SRT) Apparatus: An Effective Tool for Growing Bulk Size Single Crystals

Kiran^{1,2}, N. Vijayan^{1,2}*, Jyoti^{1,2}, Chetan^{1,2}

¹ CSIR – National Physical Laboratory, Dr. K.S. Krishnan Marg, New Delhi – 110012, India

² Academy of Scientific and Innovative Research (AcSIR), Ghaziabad- 201002, India

Received date: 17/04/2025, Acceptance date: 12/06/2025

DOI: <http://doi.org/10.63015/5c-2463.2.3>

*Corresponding Author: nvijayan.nplindia@csir.res.in

Abstract

Single crystals are emerging in technology effectively owing to their superior physical, optical and electronic properties. They serve as fundamental building blocks in advancing various domains, including optoelectronics, nonlinear optics, laser technology and photonics. One of the effective technique for growth of crystals is seed rotation method which has led to significant advancement in the controlled crystal growth process. In the present article, we provide a brief discussion on the seed rotation technique used in solution-based crystal growth methods to enhance the size and quality of crystals. The rotation reduces thermal gradients, inhibiting the emergence of defects such as dislocations and inclusions. It promotes convective mixing within the solution, hence reducing localized temperature variations and facilitating a more uniform thermal environment for the developing crystal. The enhanced thermal uniformity can indirectly mitigate the negative consequences usually linked to abrupt heat gradients, including strain and fault formation during growth. Rotation also facilitates enhanced crystal symmetry and homogeneity, which are crucial for the performance and reliability of crystals utilized in semiconductor, optical and advanced material applications. This article contains an overview on the seed rotation technique (SRT) apparatus and explores the impact of several parameters on crystal quality, as well as the mechanisms that contribute to defect reduction and enhanced structural integrity.

Keywords: single crystal, rotation, homogeneity, seed crystal, ACRT controller.

1. Introduction

Good quality single crystals are extensively needed for numerous optical devices, including electro-optical, nonlinear optical (NLO) and photo-refractive storage devices [1-3]. However, growing a good-quality crystal is often a tedious task. Most of the time, we lead to many disorders in the single crystals such as dislocations, grain boundaries, etc. There are several methods to grow a single crystal but, the low-temperature solution growth technique has its own superiority over the other methods due to its high-quality products [4-6]. It mainly requires an effective technique where different growth parameters like supersaturation level, phase homogeneity, temperature fluctuation, impurity formation and etc. can be controlled [7,8]. The slow evaporation solution technique (SEST) is considered to be the simplest and most cost-effective method for producing high-quality single crystals [9]. Although this technique is known as superior for growing highly crystalline products, still defects are created due to fluctuations in various parameters most of the time [10,11]. Similarly, the growth of various planes is blocked due to the unwanted nucleation at the walls of the growth vessel. Few of the unwanted growth of crystals are demonstrated in Fig. 1(a) which shows how crystal growth is hindered by the nucleation. From Fig. 1(b), one can observe

the damage in the crystal base plane due to uneven nature of growth vessel which results in pits on the crystal base. In order to overcome such effects, various modifications can be implemented in the existing methods and high-quality crystals can be grown with ease. In this regard, SR (Sankaranarayanan-Ramasamy) and seed rotation technique (SRT) are considered prominent for bulk-size production of single crystals [12,13]. SR method is universally adopted to grow single crystals in a particular direction. More specifically, crystals are grown across one plane known as the unidirectional growth of single crystals [14]. Whereas seed rotation allows the growth of ingot across all defined planes. All planes will evolve in their respective directions, yielding a bulk single crystal with enhanced quality as a result of controlled parameters. Rotation ensures even exposure of the seed crystal to the supersaturated solution, facilitating uniform growth on all surfaces and reducing the risk of asymmetrical or faceted growth. In both the later said techniques, crystals are grown in a more controlled way to minimize the defect concentration and maximise the yield [15-17]. We will discuss the seed rotation technique and the effect of various controlled parameters on the growth of single crystals in this article. Details on the apparatus of the seed rotation method will be described in the forthcoming section.

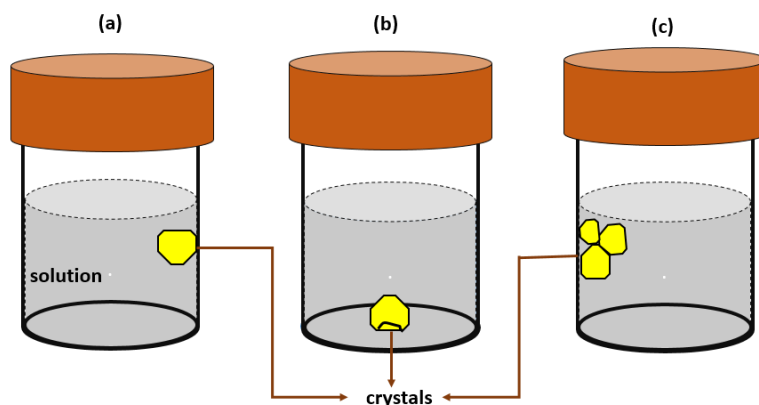


Figure 1 (a) Plane stuck on the walls of the beaker, (b) Hampered plane due to base of the beaker and (c) The formation of aggregates leading to multinucleation.

2. Design and Operation of SRT Apparatus

“SRT” is one of the most significant low-temperature solution growth technique which is used to grow high-quality and bulk-size single crystals [18-21]. Generally, parameters like supersaturation, solubility, temperature fluctuation and mechanical vibrations are significant in SEST [22]. When evaporation takes place, solute molecules settle at the bottom of the growth vessels. Therefore, the homogeneity of the solution is automatically lost, as a result of this, uniform growth of crystals is hampered. In order to overcome such difficulties, SRT is used which provides an extra parameter i.e. ‘rotation’ to maintain the uniform growth of the crystal. Gradually rotating the platform containing seed crystal during the growing phase facilitates a symmetrical distribution of temperature and solute concentration around the seed crystal. This will help in reducing the inhomogeneities present in the solution. In this way, it helps in maintaining a steady concentration of solute near the crystal surface by preventing local accumulation, which is crucial for sustaining constant growth rates.

Recently, we installed an ‘SRT’ setup at CSIR-National Physical Laboratory, New Delhi, India. The detailed setup is provided in Fig. 2 which consists of a seed rotation controller coupled with a stepper motor (controlled by using a microcontroller-based drive (ACRT controller)), a glass beaker (5 Litre) and a crystal holder with the motor shaft connecting to ACRT controller. The ACRT (which means automatic crystal rotation and translation) controller plays a vital role in the seed rotation system by offering precise, programmable control over the movement of the seed crystal through the crystal growth process. The system described here provides a maximum rotation speed of 77.9 RPM (revolutions per minute) and a minimum speed of 0.1 RPM. It has three modes of operation 1. auto mode, 2. manual

mode and 3. acceleration/ de-acceleration mode. In the auto mode, the motor runs continuously for the set RPM and direction of rotation can be set either clockwise or anticlockwise. In this mode, the controller regulates the rotation speed of the seed crystal as per the set rpm, ensuring a uniform and optimized rotational motion throughout the growth period. In the manual mode, we can manually set the number of cycles, and run the motor in two different modes: fixed mode and BI direction mode. In fixed mode, the motor shaft starts running at fixed RPM in clockwise/anticlockwise direction for desired number of cycles and then motor stops. In the bidirectional mode, initially motor shaft starts running in the forward (clockwise) direction for the desired number of cycles. On completing forward cycle, shaft starts rotating in reverse (anticlockwise) direction for the same number of cycles and then motor stops. The main benefit of manual mode is user can directly control the setting parameters as per requirement in a more optimized way during the growth process. It can help in a controlled growth process and one can get better quality of the crystal. In the third mode that is acceleration/ de-acceleration mode, the speed X (RPM) of motor and time (t) for which that X has to be maintained can be set for required number of cycles. Acceleration denotes how quickly the controller increases the rotation speed from zero (or a lower value) to the set value whereas de-acceleration is how gradually it slows the movement down before stopping. It facilitates controlled and predictable movement, which is especially crucial when handling fragile or delicate seed crystals. The choice between acceleration/de-acceleration mode and continuous rotation typically depends on the desired control over convection and solute distribution. Acceleration/de-acceleration mode entails periodic variation of the rotational speed. This sporadic motion can improve convective mixing around the seed and throughout the

solution, aiding in the prevention of localized supersaturation. This is often applied in the growth of crystals with complex compounds, where segregation and striation control are critical. In contrast, continuous rotation is favoured when a consistent and uniform convective flow is

needed for processes like the development of high-purity single-component crystals. In this way, we can optimize the settings according to our requirement and obtain a good quality bulk single crystal useful in many applications [23-25].

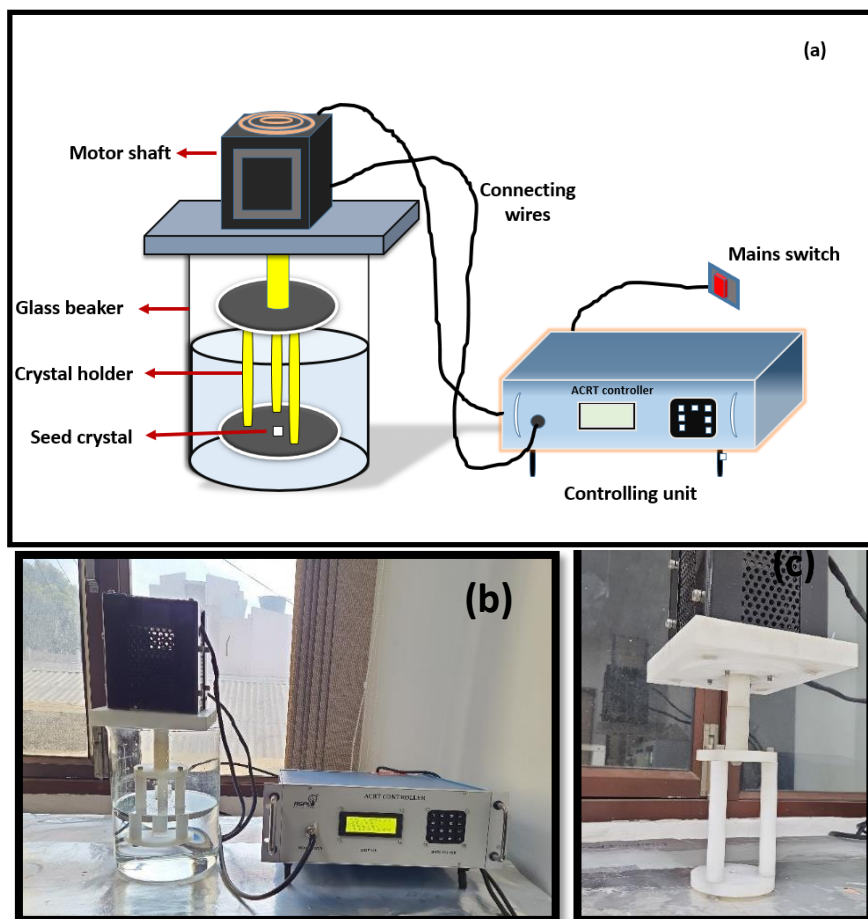


Figure 2 (a) Schematic diagram of seed rotation (SRT) setup, (b) Complete setup of SRT at CSIR-NPL, New Delhi and (c) Crystal holder with seed mount on the platform.

3. Working Procedure

In this technique, first we require a seed crystal which is produced using conventional slow evaporation solution technique (SEST). The seed crystal must be free from inclusions, cracks, or twin boundaries and size of the crystal should be sufficient to initiate growth (typically 3-10 mm) with well-developed natural facets. It is then lapped and polished with the help of alumina slurry to make flat at bottom. The final surface roughness after polishing must

be $\leq 0.1 \mu\text{m}$ and force applied should be 1–2 N (gentle to avoid microfractures). The SRT apparatus is then used to grow the bulk size single crystal. At first, a saturated solution of the same material is prepared following the SEST procedure with the temperature range determined by its solubility curve [4,18]. The saturated solution is poured in the glass beaker with the help of funnel only after filtration in order to remove undissolved particles or dust that could act as unintended nucleation

centers. Ensure the beaker in which solution is poured is thoroughly cleaned and rinsed with the same solvent used in the preparation of the solution. The solution should be slowly transferred along the side of the beaker to minimize turbulence, avoid bubble formation, and prevent localized cooling or splashing. Crystal holder made up of teflon is dipped in this solution after pasting the seed crystal on its surface as seen in Fig. 2(a). The quantity of the saturated solution in the beaker should be made such that it should cover some portion of the crystal holder as shown in Fig. 2(b). The stepper motor is paired with a seed (crystal) holder where the seed crystal is kept for crystallization. This motor rotates the seed holder in the crystallizer. The seed crystal is put in the centre of the platform and fixed with the help of adhesive to avoid disturbance. The adhesive Anabond 202 can be used which is a non-reactive material to avoid any kind of impurity in the solution. The crystal holder rotates along with the motor shaft according to the commands that motor shaft receives from the controller unit (ACRT controller) via the connector [26]. The ACRT controller controls the rotation motor settings. It has a LED display where we can see the stepper motor settings and set accordingly. This makes SRT an effective tool which can be made even more impactful by various controlled factors. The set up should be kept in a controlled environment for the growth process. The impact of various parameters during the growth part will be discussed in the next section.

4. Impact of different parameters

By utilizing seed rotation technique, various growth parameters such as growth atmosphere and rotation rates under the fixed growth rate can be optimized which will help in production of high quality bulk single crystals. The effect of rotation plays vital role in the growth part. Rotation will provide uniformity to the solution making it stable which in turn will help in the uniformity in the single crystal. Inclusions

in the crystals will occur as a result of inhomogeneous supersaturation in the solution, which is why the seed must rotate uniformly to prevent stationary areas or recirculating flows. This will give crystal with minimum inhomogeneity which mainly includes dislocations, strains, grain boundaries, etc. Also, it is important to optimize the speed of the motor as the rotation speed also plays an important role in improving the crystal quality. It was found that when the solution was stirred by rotating the seed crystal at 10 rpm in the anticlockwise direction, due to stability in the solution the crystal quality was improved. Hence, the importance of optimum rates of rotation in crystal growth processes has significantly lead to improved quality. Conversely, if not well controlled, rotation can cause uneven solute concentration around the seed, leading to striations or irregular crystal shape. High-speed or fluctuating rotation in some cases can induce mechanical vibrations or misalignment, leading to growth instabilities or off-axis crystal development. Therefore, it is crucial to manage rotation parameters carefully to avoid such disruptions. In addition to this, in systems with a high solvent evaporation rate, rotation can accelerate solvent loss or disrupt the meniscus, making the process unstable. In these instances, seed rotation is less relevant, and alternative growth strategies are preferred.

Thermal fluctuations due to natural convection can also be controlled to stabilize the solution. Controlled atmosphere can be maintained by providing constant temperature to the solution. In order to maintain constant temperature of the solution, the beaker attached with crystal holder is kept in the constant temperature bath (CTB) which can help optimize the temperature as depicted in Fig. 3. The crystal can be extracted from the solution once the desired crystal size and quality are attained, following a progressive reduction or cessation of the heating

process to provide controlled cooling. The crystal is then separated from the seed holder and removed from the apparatus for post-growth processing, including cutting, polishing, or characterization. The sulphamic acid crystal grown by Sonia *et al.* and corundum single crystals grown by K. Watanabe, *et al.* using the seed rotation technique are the well-known examples [27,13]. Among these, the sulphamic acid single crystal obtained using seed rotation technique possess dimensions $40 \times 10 \times 23 \text{ mm}^3$ which was produced with a seed crystal of dimensions $10 \times 3 \times 7 \text{ mm}^3$. These examples underscore the versatility and efficacy of seed rotation in improving the quality of various functional crystals in optical, electrical, and photonic applications [28,29].

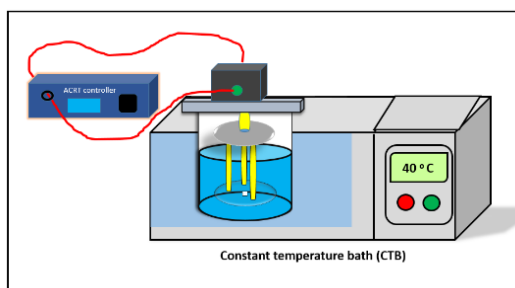


Figure 3 Constant temperature bath (CTB) to maintain growth atmosphere stable.

5. Conclusion

In conclusion, the seed rotation technique (SRT) apparatus represents a significant advancement in crystal development, especially for the production of bulk-sized single crystals with improved structural quality. The equipment facilitates controlled and uniform rotation of the seed crystal by efficiently minimising temperature and chemical gradients at the growth interface, hence decreasing the probability of defect formation and fostering uniform crystal development. Its adaptability to several crystal growth techniques and materials makes it a

versatile tool for both research and industrial applications.

Conflicts of Interest

There are no conflicts to declare.

Acknowledgements

All the authors in this article are grateful to the Director, CSIR-NPL, New Delhi for providing such a facility to grow single crystals and persuading Ph.D. in ACSIR. One of the authors Ms. Kiran is grateful to CSIR, India for the financial support through CSIR- Senior Research Fellowship (SRF) and ACSIR-NPL, India for PhD registration.

References

- [1] P.S. Patil, S.R. Maidur, S.V. Rao, S.M. Dharmaparakash, Crystalline perfection, third-order nonlinear optical properties and optical limiting studies of 3,4-Dimethoxy-4'-methoxychalcone single crystal, *Opt. Laser Technol.* 81 (2016) 70–76.
- [2] L. Zhao, S.B. Li, G.A. Wen, B. Peng, W. Huang, Imidazole derivatives: Thermally stable organic luminescence materials, *Mater. Chem. Phys.* 100 (2006) 460–463.
- [3] M. Narayan Bhat, S.M. Dharmaparakash, Growth of nonlinear optical γ -glycine crystals, *J. Cryst. Growth* 236 (2002) 376–380.
- [4] Kiran, N. Vijayan, D. Nayak, M. Kumari, Vinod, K. Kumar, P. Vashishtha, N. Thiruganasambantham, V. Balachandran, B. Sridhar, G. Gupta, A comprehensive assessment on synthesis, growth, theoretical & optical properties of glycine zinc sulphate pentahydrate single crystal for third-order nonlinear optical applications, *J Mater Sci: Mater Electron* 34 (2023) 1132.

- [5] B. Simon, R. Boistelle, Crystal growth from low temperature solutions, *J. Cryst. Growth* 52 (1981) 779-788.
- [6] R.A. Laudise, *Techniques of crystal growth*, Appl. Solid State Phys. Boston, MA: Springer US, (1970) 171-178.
- [7] S.A. Gandhi, Single crystal growth by a slow evaporation technique: Concept, mechanisms and applications, *CRYSTAL GROWTH* (2017) 1.
- [8] K. Byrappa, T. Ohachi, *Crystal growth technology*, Elsevier, 2003.
- [9] A. Badoni, Kiran, N. Vijayan, D. Joshi, Jyoti, K. Kumar, S. Srivastava, J. Prakash, Analysis on optical, thermal and third-order nonlinear properties of L-histidine hydrochloride monohydrate single crystal, *Phys. Scr.* 99 (2024) 105959.
- [10] W.R. Wilcox, Removing inclusions from crystals by gradient techniques, *Industrial & Engineering Chemistry* 60.3 (1968) 12-23.
- [11] Kiran, N. Vijayan, N. Sarkar, D. Joshi, Jyoti, K. Kumar, S. Yadav, S. Das, Unveiling the optical, thermal and nonlinear behavior of guanidinium benzenesulfonate: A promising organic single crystal for NLO applications, *Opt. Mater.* 147 (2024) 114683.
- [12] M. Kumari, N. Vijayan, D. Nayak, Kiran, J. S. Tawale, P. Singh, R. P. Pant, Investigation on unidirectionally grown $\langle 010 \rangle$ potassium acid phthalate single crystal by Sankaranarayanan–Ramasamy (SR) method for optical applications, *Appl. Phys. A* 127 (2021) 780.
- [13] K. Watanabe, A. Iida, Y. Sumiyoshi, Growth of corundum single crystals by seed rotation method, *J. Cryst. Growth.* 54 (1981) 381—393.
- [14] K. Sankaranarayanan, Growth of large size $\langle 1\ 1\ 0 \rangle$ benzophenone crystal using uniaxially solution-crystallization method of Sankaranarayanan–Ramasamy (SR), *J. Cryst. Growth.* 284 (2005) 203-208.
- [15] C. Fang, S. Liu, Y. Wen, M. Chen, N. Wang, W. Luo, Y. Feng, H. Yao, Heng-Yun Ye, L. Liu., Dynamic seed rotation growth of two-dimensional perovskite single crystals for high-performance x-ray detect, *Next Materials* 2 (2024) 100137.
- [16] M.S. Pandian, U. Charoen In, P. Ramasamy, P. Manyum, M. Lenin, N. Balamurugan, Unidirectional growth of sulphamic acid single crystal and its quality analysis using etching, microhardness, HRXRD, UV–visible and Thermogravimetric-Differential thermal characterizations, *J. Cryst. Growth.* 312.3 (2010) 397-401.
- [17] C.W. Lan, Recent progress of crystal growth modeling and growth control, *Chem. Eng. Sci.* 59.7 (2004) 1437-1457.
- [18] Vikram, N. Vijayan, Ravindra, Sonia, Mahak, Apurva, Growth of KDP crystal by automatic temperature controlled seed rotation method, *Asian Journal of Physics*, 27 (2018) 13-21.
- [19] G.H. Nancollas, The growth of crystals in solution, *Adv. Colloid Interface Sci.* 10.1 (1979) 215-252.
- [20] S.A. Markgraf, Y. Furukawa, M. Sato, Top-seeded solution growth of LiB_3O_5 , *J. Cryst. Growth* 140.3-4 (1994) 343-348.
- [21] P.V. Dhanaraj, N.P. Rajesh, P. Ramasamy, M. Jeyaprakasan, C.K. Mahadevan, G. Bhagavannarayana, Enhancement of stability of growth, structural and NLO properties of KDP crystals due to additive along with seed rotation, *Cryst. Res. Technol.* 1 (2009) 54 – 60.

[22] A. Mersmann, A. Eble, C. Heyer, Crystal growth, Crystallization technology handbook CRC Press, (2001) 95-158.

applications, Electron. Mater. Lett. 14 (2018) 7-13.

[23] M.S. Bakshi, A simple method of superlattice formation: step-by-step evaluation of crystal growth of gold nanoparticles through seed– growth method, Langmuir 25 (2009) 12697-12705.

[24] S. Satapathy, S.K. Sharma, A.K. Karnal, V.K. Wadhawan, Effect of seed orientation on the growth of TGS crystals with large (0 1 0) facets needed for detector applications, J. Cryst. Growth. 240 (2002) 196-202.

[25] Kiran, N. Vijayan, N. Sarkar, Vinod, Jyoti, D. Joshi, Chetan, Thermal Behaviors, Hirshfeld Surface Analysis and Impact of Shock Wave on Glycine Zinc Sulphate Pentahydrate Single Crystal, Cryst. Res. Technol. (2025) 2500016.

[26] H.J. Scheel, H. Müller-Krumbhaar, Crystal pulling using ACRT. J. Cryst. Growth. 49.2 (1980) 291-296.

[27] Sonia, N. Vijayan, M. Bhushan, K. Thukral, R. Raj, K.K. Maurya, D. Haranath, S. A. Martin Britto Dhas, Growth of a bulk-size single crystal of sulphamic acid by an in-house developed seed rotation solution growth technique and its characterization, J. Appl. Cryst. 50 (2017) 763–768.

[28] D. Nayak, N. Vijayan, M. Kumari, Kiran, P. Vashishtha, S. Das, B. Sridhar, G. Gupta, R.P. Pant, Investigation on synthesis, growth, Hirshfeld surface and third order nonlinear optical properties of Urea-Succinic Acid single crystal: A potential candidate for self-defocusing lasing application, Opt. Mater. 124 (2022) 112051.

[29] A. Saranraj, S.S. Jude Dhas, M. Jose, S.A. Martin Britto Dhas, Growth of bulk single crystals of urea for photonic



Study of p-GaN Gate HEMT's Structural and Geometrical Parameters to Realise E-mode HEMT for 750V Switch Operation

Sonalee Kapoor¹, Khuswant Sehra², Niraj Kumar¹ and D S Rawal*¹

¹Solid State Physics Laboratory, DRDO, Delhi-110054, India

²Department of Electronic Science, University of Delhi South Campus, New Delhi 110021, India

Received date: 12/06/2025, Acceptance date: 21/07/2025

DOI: <http://doi.org/10.63015/10se-2467.2.3>

*Corresponding Author: dsrawal15@gmail.com

Abstract

E-mode GaN HEMTs are the preferred device configuration for use in high power switching applications and this paper reports a TCAD study on p-GaN gate HEMT structure and device geometry to achieve high breakdown voltage for DC to DC power switching applications. Various HEMT device geometrical parameters have been studied as a function of device electrical parameters i. e. Drain current, threshold voltage R_{on} and breakdown voltage. The gate -drain spacing of greater than 10 μm is found to be the most critical dimension for achieving high breakdown voltage $\sim 750\text{ V}$ but at the cost of device current handling capability which is found to be decreasing from 960 mA/mm to 900 mA/mm when gate drain spacing of 6 μm is increased to 10 μm .

Key words: E-mode, GaN, HEMT, Drain current, threshold voltage

I. Introduction

Due to excellent properties of gallium nitride (GaN) and related alloys (e.g., $\text{Al}_x\text{Ga}_{(1-x)}\text{N}$) are promising semiconductors for the next generation of high-power and high-frequency devices. AlGaN/GaN based HEMT devices have already established dominance for the applications in MMICs and high-temperature digital ICs, due to the excellent capacity of handling high power and operating at high temperatures and are used in depletion mode device configuration. A higher energy bandgap of semiconductor leads to a higher maximum electric field blocking capability. This makes possible the reduction of the device width and therefore its on-resistance and switching times. GaN is the most promising material to achieve the lowest on-resistance and switching times due to its electron saturation velocity, electron mobility, relative permittivity and maximum electric field [1]. Minimum drift region resistance that can be obtained with GaN is about 5.7 times lower than SiC and about 2781 times lower than Si. Thus, GaN material can considerably reduce the conduction losses of the power switching devices. There are still several technological concerns hindering the complete exploitation of these materials. As an example, high electron mobility transistors (HEMTs) based on AlGaN/GaN heterostructures are inherently normally-on (a current will flow between the source and drain even at zero bias to the gate ($V_g = 0$)) devices. However, normally-off ($V_{th} > 0$) switching devices are preferred in power electronics, due to their inherent safety as they offer more failsafe operation conditions and gate driver circuitry simplicity operation. There are several methods for fabrication of normally off (enhancement mode) device, like recessed

gate, fluorine gate HEMT (consisting in the introduction of negatively charged fluorine ions below the gate electrode, either by plasma or ion-implantation processes) cascode configuration [2-4], Mainly p-GaN gate configuration is preferred for reliable switch operation due to its minimum threshold voltage invariability leading to reliable high power switching operation [5-10]. The present paper investigates the detailed simulation studies for the p-GaN gate HEMT device electrical characteristics to arrive at the optimum HEMT structure with suitable material parameters. The effect of device geometrical parameters on drain current, R_{on} and breakdown voltage is also studied to design a p-GaN gate HEMT suitable for power switching applications up to 750V.

II. HEMT structure and device layout

TCAD Simulation studies are performed to study the E-mode HEMT device characteristics using ATLAS device simulator [11]. The effect of HEMT device geometrical parameters like gate to drain spacing (L_{gd}), gate to source spacing (L_{sd}), gate length (L_g) and gate width (W_g) on device electrical characteristics has been investigated systematically. A basic device layout is finalised as shown in fig.1 to investigate the electrical performance. p-GaN gate HEMT off state characteristics and output characteristics are simulated and analysed. Details about the structure and the simulated characteristics are presented in the following section.

The typical HEMT layer structure of p-GaN/AlGaN/GaN device is shown in fig.2 (where p-GaN : Mg as the p type impurity). To achieve an efficient depletion of the 2DEG and $V_{th} > 0$, the properties of

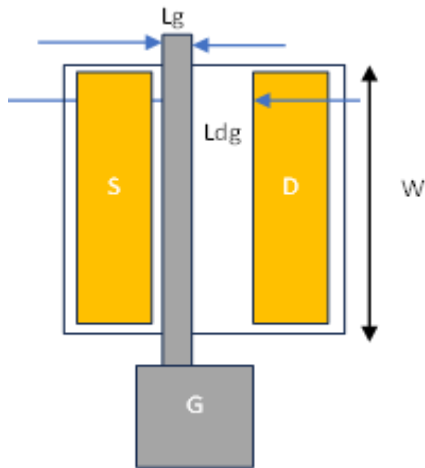


Fig.1. Basic device layout used for the study

- p-GaN:Mg, Mg~ $3E^{19}/cm^3$,
- Cap1 layer: 90nm
- GaN undoped cap2 layer: 5nm
- $Al_xGa_{(1-x)}N$ barrier: x=22% ; 18nm
- Undoped GaN channel: 500nm
- GaN buffer :3.0 μm
- AlN nucleation layer: 40 nm
- SiC substrate

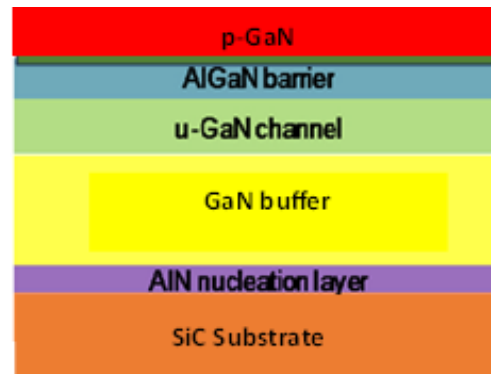


Fig.2. E-mode HEMT structure details

Table I. Device parameters used for the study

S. No	Parameter	Value (μm)
1.	Gate length, L_g	2
2.	Gate source spacing, L_{sg}	2
3.	Gate drain spacing, L_{gd}	4, 6, 10, 12
4.	p-GaN length, L_p	4
5.	Gate width, W_g	100
6.	p-doping	$3 \times 10^{19} cm^{-3}$

TCAD simulation studies were carried out by selecting a basic device layout and authenticated by using ATLAS device simulator. The simulation deck was calibrated using published experimental

normally-off p-GaN/AlGaIn/GaN heterostructure the AlGaIn barrier layer thickness is in the range of 10–18 nm, while the Al concentration is in the order of 18-22% and high doping level of the p-GaN layer ($> 10^{18} cm^{-3}$) is also required for an efficient depletion of the region at the metal-gate/p-GaN interface. A typical e-mode hetero-structure with top p-GaN layer of 80-90nm thickness was chosen to completely deplete the channel under the p-GaN gate at zero gate voltage.

result in IEEE EDL-42, pp-22, Jan 2021[12]. The device parameters used for simulation are given in table I. The device geometrical parameters are selected based on the presently existing fabrication capability inhouse.

III. Results and Discussion

In the lateral device like GaN HEMT, in addition to material parameters like 2DEG density (N_s), carrier mobility (μ) and sheet resistance (R_s), the device geometrical parameters i.e. gate to drain spacing (L_{gd}), gate to source spacing (L_{sd}), gate length (L_g) and gate width (W_g) are very critical for achieving desired device DC characteristics. The effect of these

geometrical parameters has been studied in detail on device electrical characteristics and results are presented below.

A. Transfer Characteristics at $V_{ds} = 10$ V: The drain current (I_{ds}) is showing direct dependency on L_{gd} and decreasing with its increase mainly due to increase in source drain resistance. The maximum value of current obtained is ~ 0.96 A/mm at $L_{gd}=4 \mu\text{m}$ and is clearly shown in fig. 3.

- Red - L_{gd} : $4 \mu\text{m}$ ($I_{d-\text{Max}}$: 0.96 A/mm)
- Green - L_{gd} : $6 \mu\text{m}$ ($I_{d-\text{Max}}$: 0.94 A/mm)
- Blue - L_{gd} : $10 \mu\text{m}$ ($I_{d-\text{Max}}$: 0.92 A/mm)
- Sky Blue - L_{gd} : $12 \mu\text{m}$ ($I_{d-\text{Max}}$: 0.90 A/mm)

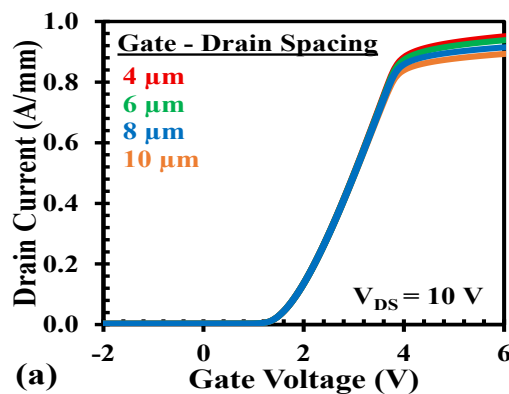


Fig.3. Drain current (I_{ds}) as a function of gate drain spacing (L_{gd})

B. Output Characteristics: Fig.4 shows the simulated device output characteristics as function of L_{gd} which clearly indicates increase in R_{on} with increase in L_{gd} .

- Red - L_{gd} : $4 \mu\text{m}$
- Green - L_{gd} : $6 \mu\text{m}$
- Blue - L_{gd} : $8 \mu\text{m}$
- Sky Blue - L_{gd} : $10 \mu\text{m}$

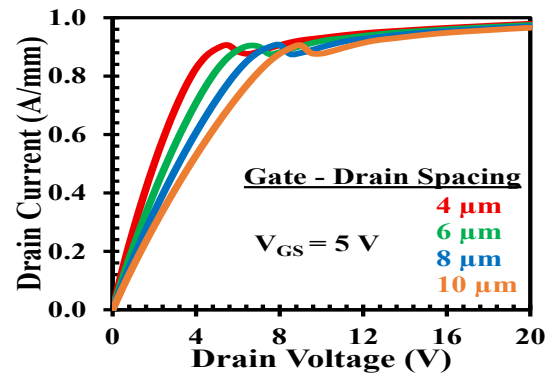


Fig.4. Simulated device output characteristics

C. Output Characteristics for L_{gd} : $4 \mu\text{m}$ as a function of gate source voltage:

Fig.5 shows the variation of output characteristics as a function of gate source voltage. The graph clearly indicates that the saturated I_{ds} current is increasing with gate voltage due to increase in channel opening as result of reduction in depletion region under gate.

- Blue: $V_{gs} + 5$ V
- Green: $V_{gs} + 3$ V
- Red: $V_{gs} + 1$ V

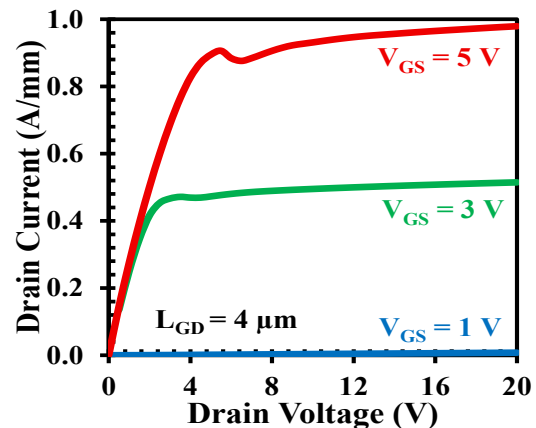


Fig.5. Variation of output characteristics as a function of gate source voltage (V_{gs}).

D. Impact of gate drain spacing (L_{gd}) on Breakdown voltage: Fig. 6 depicts effect on L_{gd} on V_{boff} that represents breakdown voltage in device off-state condition, and is one of the very critical parameter for power switching application. It clearly shows the strong dependency of breakdown voltage on L_{gd} and increases with increase in L_{gd} . The

desired breakdown of $> 750\text{V}$ is achieved for the $L_{gd} \sim 10\text{ }\mu\text{m}$.

- Red - L_{gd} : $4\text{ }\mu\text{m}$ (Breakdown: 480 V)
- Green - L_{gd} : $6\text{ }\mu\text{m}$ (Breakdown: 630 V)
- Blue - L_{gd} : $8\text{ }\mu\text{m}$ (Breakdown: 710 V)
- Sky Blue - L_{gd} : $10\text{ }\mu\text{m}$ (Breakdown: 750 V)

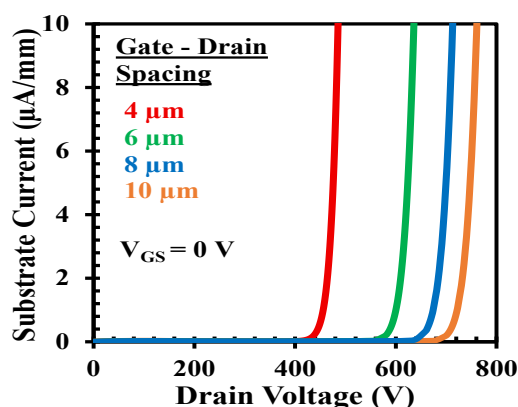


Fig. 6. Device breakdown voltage as a function of L_{gd}

The simulated results are consistent and well within the desired range. For a lateral device like HEMT, L_{gd} is very critical parameter for breakdown voltage and has been varied from $4\text{--}10\text{ }\mu\text{m}$ in current study to arrive at the optimum value of breakdown voltage $\geq 750\text{V}$ targeting EV application. This range of L_{gd} was selected to have minimum impact on device on-state device characteristics. Breakdown voltage is increasing with L_{gd} and reaches to a value $\sim 750\text{V}$ for gate drain spacings of greater than equal to $10\text{ }\mu\text{m}$. It is also worth mentioning that HEMT material parameters are equally important for achieving high breakdown voltage with good on-state device characteristics. Therefore, the thickness and Al concentration of AlGaIn barrier layer is chosen carefully to meet the requirement of reasonable 2DEG density $\geq 8 \times 10^{12}\text{ cm}^{-2}$ and mobility $\sim 1800\text{ cm}^2/\text{V. sec}$.

Conclusions

A p-GaN gate HEMT device basic layout/structure has been optimised using TCAD simulation. Several HEMT device geometrical parameters have been studied and a basic device layout has been finalized. The device electrical parameters are strong function of HEMT material and device geometrical parameters. It is also evident from the simulated results that the most critical parameter for power switch i.e. breakdown voltage is greatly influenced by gate to drain spacing in a lateral device like GaN HEMT. The L_{gd} spacing of greater than $10\text{ }\mu\text{m}$ is an essential requirement in E-mode HEMT for achieving high breakdown voltage $\sim 750\text{V}$ but at the cost of device on state performance that gets affected in terms of increased R_{on} . Therefore, it is essential to minimize L_{gd} in the device layout while maintaining the desired breakdown.

Acknowledgements

The authors would like to thank GaN Team and Director SSPL, DRDO, Delhi for the valuable support and guidance to carry out the work.

References

- [1]. K.J. Chen, et al., GaN-on-si power technology: devices and applications, IEEE Trans. Electron Devices 64 (3) (March 2017) 779–795, <https://doi.org/10.1109/TED.2017.2657579>.
- [2] W. Saito, Y. Takada, M. Kuraguchi, K. Tsuda, I. Omura, Recessed-gate structure approach toward normally off high-voltage AlGaIn/GaN HEMT for power electronics applications, IEEE Trans. Electron Devices 53 (2) (Feb. 2006) 356–362, <https://doi.org/10.1109/TED.2005.862708>.

- [3] Yong Cai, Yugang Zhou, K.J. Chen, K.M. Lau, High-performance enhancement-mode AlGa_N/Ga_N HEMTs using fluoride-based plasma treatment, *IEEE Electron Device Lett.* 26 (7) (July 2005) 435–437, <https://doi.org/10.1109/LED.2005.851122>.
- [4] S. Huang, et al., High uniformity normally-OFF Ga_N MIS-HEMTs fabricated on ultra-thin-barrier AlGa_N/Ga_N heterostructure, *IEEE Electron Device Lett.* 37 (12) (Dec. 2016) 1617–1620, <https://doi.org/10.1109/LED.2016.2617381>.
- [5] O. Hilt, A. Knauer, F. Brunner, E. Bahat-Treidel, J. Würfl, Normally-off AlGa_N/Ga_N HFET with p-type Ga_N Gate and AlGa_N buffer, in: *IEEE International Symposium on Power Semiconductor Devices & IC's*, June 2010, pp. 347–350.
- [6] Y. Uemoto, et al., Gate injection transistor (GIT)—a normally-off AlGa_N/Ga_N power transistor using conductivity modulation, *IEEE Trans. Electron Devices* 54 (12) (Dec. 2007) 3393–3399, <https://doi.org/10.1109/TED.2007.908601>.
- [7] I. Hwang, et al., p-Ga_N gate HEMTs with tungsten gate metal for high threshold voltage and low gate current, *IEEE Electron Device Lett.* 34 (2) (Feb. 2013) 202–204, <https://doi.org/10.1109/LED.2012.2230312>.
- [8] F. Lee, L. Su, C. Wang, Y. Wu, J. Huang, Impact of gate metal on the performance of p-Ga_N/AlGa_N/Ga_N high electron mobility transistors, *IEEE Electron Device Lett.* 36 (3) (March 2015) 232–234, <https://doi.org/10.1109/LED.2015.2395454>.
- [9] X. Liu, et al., Normally-off p-Ga_N Gated AlGa_N/Ga_N HEMTs using plasma oxidation technique in access region, *IEEE J. Electron Devices Soc.* 8 (Feb. 2020) 229–234, <https://doi.org/10.1109/JEDS.2020.2975620>.
- [10] X. Li, et al., Observation of dynamic VTH of p-Ga_N gate HEMTs by fast sweeping characterization, *IEEE Electron Device Lett.* 41 (4) (April 2020) 577–580, <https://doi.org/10.1109/LED.2020.2972971>.
- [11] Silvaco atlas TCAD tool ver. 5.28.1.R. User's manual Available at: <https://www.silvaco.com>.
- [12] L. Zhang, Z. Zheng, S. Yang, W. Song, J. He, K.J. Chen, p-Ga_N gate HEMT with surface reinforcement for enhanced gate reliability, *IEEE Electron Device Lett.* 42 (1) (Jan. 2021) 22–25, <https://doi.org/10.1109/LED.2020.3037186>.



Classification and Analysis of 12-Lead Electrocardiograms

Revanth Reddy Pasula

Department of Computer Science, Wichita State University, Wichita, United States

Received date: 01/07/2025, Acceptance date: 21/07/2025

DOI: <http://doi.org/10.63015/2ai-2471.2.3>

*Corresponding Author: revanthreddy210799@gmail.com

Abstract

This work investigates the classification of 12-lead electrocardiogram (ECGs) to detect abnormalities in the heart using three computational techniques. They are: (1) gradient-boosted ensembling following manual feature extraction, (2) deep learning with stacked autoencoders connected to the output of a multi-layer perceptron (MLP) classifier, and (3) a fusion model combining deep-learning and manually extracted features. An experiment is conducted using the PhysioNet/Computing in Cardiology Challenge 2020 database, addressing a multi-label classification task involving 27 heartbeat rhythm diagnoses. The best-performing model, which merges handcrafted features with autoencoder-derived features, achieves an average classification accuracy of 30.7% and a challenge metric score of 0.4366. The paper concludes by discussing potential improvements in multi-channel ECG classification methods.

Keywords: ECG Classification; 12-Lead ECG; Feature Extraction; Deep Learning; Autoencoders; Gradient Boosting

I. INTRODUCTION

Cardiac conditions still top the global causes of death at approximately 80% of deaths related to them, mainly due to heart attack and stroke. Twelve-lead electrocardiography (12-lead ECG) is the key to detecting cardiac pathology and assessing high-risk patients. An ECG captures the heart's electrical signals from electrodes positioned on the chest and limbs, producing waveforms corresponding to myocardial depolarization and repolarization. While computer-aided ECG analysis is widely adopted, current automated interpretation software sometimes fails to match the accuracy of specialist cardiologists, leading to missed or incorrect diagnoses. Technological advances have introduced a variety of ECG recording devices, ranging from portable single-lead designs to sophisticated clinical machines. Consumer-oriented devices like the a six-lead model, Apple's one-lead Apple Watch, and the three-lead Cardio Core wearable demonstrate the growing potential for personalized heart monitoring. However, in clinical settings, standard 12-lead systems produced by manufacturers such as General Electric and Philips remain the gold standard for comprehensive cardiac evaluation. This paper focuses on the traditional 12-lead ECG, which provides extensive coverage of cardiac electrical signals from various directions and is widely used in clinical practice. This study proposes a framework that integrates conventional signal processing with modern machine learning techniques for multi-label classification of 12-lead ECG data. It emphasizes three distinct modelling approaches for automated detection of various cardiac conditions from ECG signals. The study's hypotheses are framed based on these approaches:

- **Hypothesis 1:** Classic machine learning methods like gradient-boosted decision trees will perform similarly to, if not better than, deep learning methods (using autoencoders) in cumulative metrics such as the F-measure and general accuracy.
- **Hypothesis 2:** For tree-structured classifiers, systematic regularization of the input feature space and intentional feature selection will probably improve the challenge metric (a particular contest scoring criterion) better than simply augmenting the feature set with features synthesized by autoencoders.
- **Hypothesis 3:** Adding features extracted from a deep autoencoder to a decision-tree

ensemble, along with manually engineered features, is expected to improve the overall classification accuracy of the model.

II. CONTRIBUTIONS

The main contributions of this research are summarized as follows:

- **Traditional feature-based classifier:** We created a structured approach to classifying 12-lead ECG signals with deep manual feature extraction followed by an ensemble of gradient-boosted trees. It was entered in the PhysioNet/CinC 2020 Challenge [11], where it attained a validation challenge score of 0.476 and a test (hidden set) score of -0.080, ranking 36 out of 41 valid submissions in the official ranking.
- **Deep learning autoencoder classifier:** We employed a deep learning approach using stacked autoencoders to obtain concise representations from segmented heartbeats and then a sequence model to predict full ECG records. Without access to official test data for this method, performance was assessed using Monte Carlo cross-validation within the public dataset (20 random 80/10/10 training-validation-testing splits). The model using autoencoder achieved an average challenge score of 0.248 on these test splits. While its overall accuracy was less than the feature-based model, the deep model yielded slightly better sensitivity to some conditions – for instance, incomplete right bundle branch block (IRBBB), left anterior fascicular block (LAnFB), prolonged PR interval, and right-axis deviation (RAD).
- **Hybrid feature-embedding ensemble:** We created a hybrid modelling approach that combines manually crafted features with feature learning from autoencoders to train an improved set of gradient-boosted tree classifiers. Compared to the purely manual method, the hybrid approach employs feature selection at the level of individual labels instead of one global ranking feature. The winning configuration, labelled “Top 1000 Features + Embeddings,” chose the top 1000 most significant features for each diagnostic label and produced a test-split challenge score of

0.4366 – well above the remaining configurations assessed within the study.

III. METHODOLOGY

Deep Autoencoder + MLP Classification (Architecture Details): In our implementation, the stacked autoencoder comprised multiple fully connected layers to encode each heartbeat segment into a low-dimensional embedding. Each heartbeat (segmented via a standard R-peak detection algorithm with a fixed window length around each QRS complex) was resampled to a uniform length (approximately 500 samples) and fed into an encoder network with three dense layers of 256, 128, and 64 neurons (using ReLU activations). The encoder's bottleneck layer produced a **64-dimensional** latent vector representing the heartbeat. A symmetric decoder (64→128→256 neurons, ReLU activations, and a linear output layer) was trained to reconstruct the input waveform from this embedding. We trained the autoencoder on the training set heartbeats for up to 100 epochs using the Adam optimizer (learning rate ~ 0.001) with mean squared error as the loss, employing early stopping if reconstruction error on a validation subset did not improve for 10 consecutive epochs to prevent overfitting. After obtaining per-beat embeddings, a sequence model was used to aggregate these into a record-level representation. Specifically, we employed a one-layer LSTM with 128 hidden units: the sequence of heartbeat embeddings for an ECG record was fed into the LSTM, and the final hidden state (128-dimensional) was taken as the record-level embedding. (We also experimented with simple averaging of the heartbeat vectors as a pooling strategy, but the trainable LSTM encoder performed comparably and retained temporal information about beat sequence.) This record-level embedding was then input to a multi-layer perceptron classifier. The MLP classifier consisted of two dense hidden layers (128 and 64 neurons, ReLU activations) and an output layer of 27 sigmoid neurons (one per diagnosis) to produce multi-label predictions. We applied a dropout rate of 0.2 in the MLP to improve generalization, and optimized the classifier using binary cross-entropy loss (with Adam, learning rate 0.001). During supervised training of the MLP, we fine-tuned the encoder and LSTM weights (which were initially learned in the unsupervised phase) – we found that allowing fine-tuning improved validation performance slightly compared to keeping the encoder frozen. The autoencoder and classifier were trained for roughly 50 epochs (with early stopping on validation loss) in each cross-validation fold. This deep architecture, including its regularization

(dropout and early stopping), was designed to balance model complexity with the risk of overfitting. The result was an end-to-end deep network that first compresses beats into latent features and then learns to classify entire ECG records from sequences of those features. However, as discussed later, this complex model did not outperform the simpler approaches.

IV. RESULTS

A Comparison of classification performance metrics on the test split for the XGBoost ensemble across different feature selection strategies is shown in Figure 1. The horizontal axis labels “A” through “J” correspond to the ten model configurations detailed in Table I (in order). Plotted values include the PhysioNet Challenge score (the primary metric) alongside secondary metrics such as overall accuracy and F1-score, all summarized over 20 cross-validation runs. Each colored marker, along with its error bar or box, shows the distribution (mean and variance) of a given metric for each configuration. The figure highlights the trade-offs in performance when using all features, the top-1000 features, or the top-100 features, with and without incorporating autoencoder embeddings.

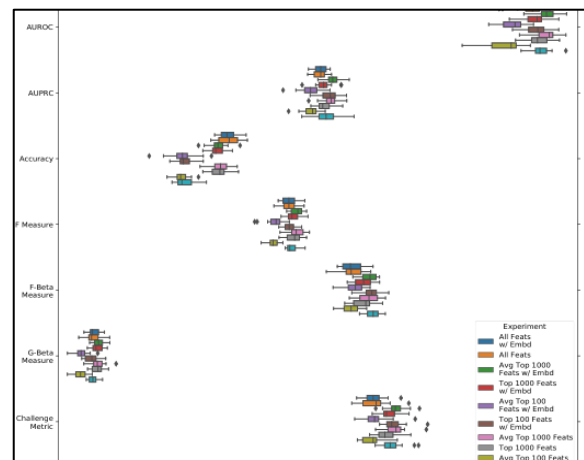


Fig 1. Comparison of classification performance metrics.

The Output of the Wilcoxon signed-rank test analyzing the distributions of the Challenge metric for all pairs of model configs is shown in Figure 2. The entry in the matrix is the p-value for the null hypothesis the corresponding pairs of configs' performance is the same; darker hues represent lower p-values. The cells marked by the symbol (*) correspond to statistically significant differences at $\alpha = 0.001$. For example, configs with aggressive feature pruning by selecting Top 100 features have different configuration performance than some others ($p < 0.001$ in those rows), uncovering the impact of the feature selection approach. Smaller p-values in

general (dark blue cells in the heatmap) reflect configuration pairs where the performance had differed significantly, uncovering the modelling choice (label-specific selection of features, including embeddings, etc.) with the resultant impact on the Challenge score.

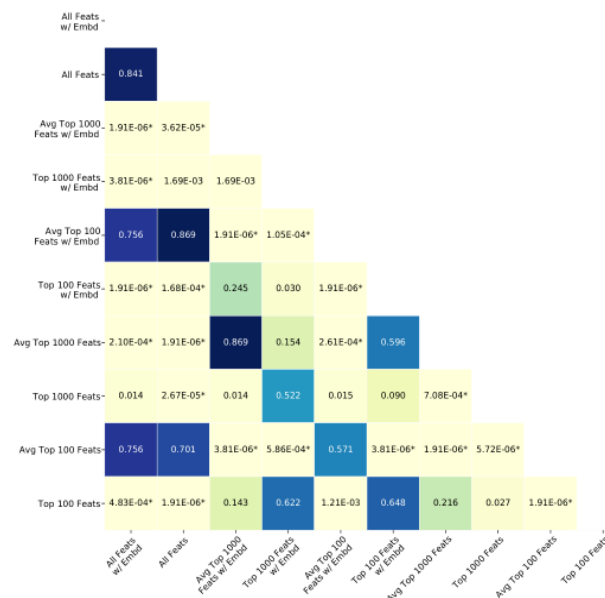


Figure 2. Wilcoxon signed-rank test distributions

V.DISCUSSION

The findings of our research emphasize a few key points, consistent with observations by other researchers. First, the inclusion of automatically learned deep features did not yield a performance gain, in line with comments by Bengio et al. that simply adding deep models to standard machine learning pipelines may not improve results. In our case, the gradient boosting ensemble achieved strong results with carefully selected time-domain and morphological features alone, and the added complexity of the autoencoder-derived features did not pay off in improved scoring. One likely reason is that the unsupervised autoencoder learned latent features that were not well aligned with the discriminative features needed for classification – the tree models could not effectively utilize the extra information when those deep features were essentially abstract combinations of raw signals. Furthermore, using deep features as input to a shallow classifier reduced interpretability of the system; it became difficult to trace which ECG lead or waveform characteristic contributed to a given autoencoder feature, obscuring the reasoning behind a particular prediction.

Several factors may explain why the autoencoder-based deep model underperformed the traditional feature-based model. Model depth and complexity:

The deep autoencoder and LSTM introduced a large number of trainable parameters, increasing the risk of overfitting given the effective amount of labelled training data (43,000 records – substantial, but small relative to the complexity of a deep network). Training the autoencoder to reconstruct signals, while useful for unsupervised feature learning, does not guarantee that the learned features are optimal for distinguishing arrhythmias. The deep model might require even more data or more aggressive regularization to realize its potential, whereas the simpler XGBoost models could generalize well with the available data. Over-compression bottleneck: By compressing each heartbeat (hundreds of sample points) into a 64-dimensional code and then compressing an entire sequence of beats into a 128-dimensional record vector, the autoencoder may have discarded subtle but important information needed to differentiate certain diagnoses. This information bottleneck can hurt classification – for example, fine-grained timing differences or low-amplitude waveform nuances might be lost in the compression. Mismatch between learned vs. discriminative features: The autoencoder was optimized to minimize reconstruction error, not to maximize classification accuracy. Thus, it likely learned features capturing dominant morphological patterns (to faithfully rebuild signals) rather than the specific anomalies that signal different arrhythmias. Those latent features could be “orthogonal” to the features that best separate classes, making it hard for the MLP (or the hybrid model’s trees) to translate them into better predictions. In short, the deep model’s abstract features did not add significant new predictive signal beyond what the manually engineered features already provided. Consequently, we failed to support Hypothesis 3 – incorporating unsupervised deep features did not significantly enhance classification accuracy or the Challenge metric in this study.

Another important aspect is data quality. The public ECG dataset had several limitations that we did not fully address in preprocessing, and these likely affected all models’ performance. There was evident label noise and inconsistency – for example, some records were clearly bradycardic (heart rate < 60 bpm) yet not labelled as such, and there were cases of low-voltage QRS complexes being labelled as atrial fibrillation or other rhythm abnormalities. We also observed instances where the distinction between atrial fibrillation and atrial flutter was inconsistently labelled. Such mislabels (or missing labels for certain conditions) introduce confusion during training: the classifiers might learn to predict “incorrect” patterns or ignore certain abnormalities because they are not reliably annotated. Additionally, the ECG signals

showed significant artifacts in some cases – e.g., baseline wander that led to unrealistic voltage shifts, or extremely low signal-to-noise ratios where true P/QRS/T waves were barely discernible. We did not perform advanced filtering or artifact removal beyond basic normalization, meaning the models had to cope with this noise. These dataset issues (noisy signals, missing or incorrect labels) likely prevented higher accuracy. Even an ideal algorithm would struggle if some arrhythmias are unlabelled or if noisy recordings are present with misleading labels. In future work, refining the dataset by removing or relabelling questionable records and reducing artifacts could lead to overall improvements in model performance. Ultimately, the limitations of the training data – including label noise, incomplete annotation of certain arrhythmias, and various ECG artifacts – constrained the accuracy achievable by both the shallow and deep learning approaches. We recognize that our choice to apply minimal preprocessing was a trade-off: it preserved data quantity and variability but came at the cost of introducing more noise. Addressing these data quality challenges will be essential to further enhance model performance. Lastly, we note that our choice of classifier and feature set also influences outcomes. We used gradient-boosted trees (XGBoost) for the feature-based models due to their robust handling of high-dimensional data and strong performance in many settings. It would be valuable to explore whether other classifiers (e.g., SVMs or random forests) using the same manual feature set could achieve similar results – perhaps the boosted trees had no special advantage beyond being well-tuned for this task. Moreover, our manual feature generation yielded thousands of features using general time-series libraries. While this broad approach helped initial performance, it likely included redundant or irrelevant features. A more targeted feature design using clinical expertise (focusing on known ECG markers for each condition) could produce a smaller, more interpretable feature set that rivals the larger set in accuracy. This could improve efficiency and transparency, as the model would rely on medically meaningful features.

VI. CLINICAL IMPLICATIONS

From the clinical point of view, the study shows the promise and the limitations of automated ECG classification. The algorithms were more accurate in some cardiac conditions than others. Notably, conditions with specific waveform changes were identified more reliably. For instance, bundle branch blocks and axis deviations – conditions with definite morphological changes in ECG – were some of the best-identified conditions. The deep-learning model

had modestly higher sensitivity for conditions like incomplete right bundle branch block (IRBBB), left anterior fascicular block (LAFB), prolonged PR interval, and right-axis deviation than the feature-based one. This makes sense, because these conditions affect specific intervals or waveforms (e.g., the QRS shape for IRBBB, the measurable interval of the PR for prolonged interval) that the algorithms – more specifically the autoencoder – were tuned to identify. When compared with other scenarios, the models underperformed in situations of mild, transient arrhythmia or otherwise noise-influenced situations. For example, separating atrial fibrillation from atrial flutter or other atrial 'arrhythmias proved challenging partly due to inaccurate categorizations in the datasets the models were trained on and partly because underlying features of AF (such as an irregularly irregular rhythm and an absence of P-waves) could easily be obscured or masked by noise or other atrial activity. Likewise, conditions of low-amplitude T-wave abnormalities or subtle ischemic changes were the most difficult to identify because they involve the detection of fine waveform variations neither captured adequately by our features nor by the autoencoder. Occasionally, the algorithms would make erroneous predictions – for instance, identifying a record to have a “T-wave abnormality” where the signal was noisy and where there were no visible T-waves, revealing likely false alarms caused by artifacts. Generally, high-amplitude or timing-based abnormalities (e.g., blocks and axis shifts) were more easily identified by the algorithms than were rhythm disorders or low-voltage changes hidden in noise. Balancing false alarms and missed events is important in evaluating clinical utility. Our top-performing model – a hybrid ensemble – tended to favor sensitivity for some diagnoses due to the weighting of the challenge metric. This caught more cases of severe arrhythmias but resulted in some false alarms. For instance, the model sometimes marked recordings as atrial fibrillation where irregularity resulted from motion artifacts. Such false alarms might result in unwarranted testing were it to be used in clinical practice. Misclassifications were also seen in recordings where baseline wander or noise was severe – the model outputted AF, atrial flutter, or “T-wave abnormality” where no actual arrhythmia was present. Left uncontrolled, these false alarms might lead to alarm fatigue in clinical environments. Conversely, the models at times missed arrhythmias detected by the cardiologist – e.g., infrequent premature beats or minor ST-segment shifts in ischemia suspicion. Incidentally, some records with overt bradycardia (severely slowed heart rate) were neither marked nor detected by the model,

presumably because bradycardia was sporadically tagged in the training material. Omitting such important events (false negatives) is especially troublesome in medicine because it would result in the patient's clinical status being undertreated. Though we did not report sensitivity for life-threatening arrhythmias *per se* because the setup is multi-label, the modest total sensitivity suggests some clinically significant events would routinely be omitted by the model in its present incarnation. It's also important to interpret the metrics of the performance in context. Our top model obtained around 30.7% overall accuracy in the test-split, by which we mean the complete list of multi-label diagnoses was correct in approximately one-third of cases. At first, 30% accuracy might appear poor in comparison to the average single-label task. All the same, in the multi-label classification task of 27 possible diagnoses, this is not directly comparable to 90% accuracy in e.g. the two-class task. The random guess or the frivolous classifier would obtain way below 30%, hence the model is undoubtedly extracting signal from the information. Nonetheless, from the clinical point of view, 30% accuracy (as well as the Challenge score of ~ 0.4366) is way from being enough for one's own diagnostic usage. In practice, it would mean the algorithm's output set of diagnoses for an ECG would be correct in the full set simply less than one-third of the time – quite insufficient for clinical decision-making. Doctors cannot tolerate missing 70% of the diagnoses or tolerating constant false alarms in the everyday workflow. At the current performance level, the model is best thought of as a decision support tool instead of an independent diagnostic system. For instance, model performance could pre-screen or flag some ECGs; even at 30% accuracy level, the model may mark ECGs as potentially abnormal for further consideration or provide a suggested list of conditions for clinicians to consider. This may highlight cases that may go otherwise unnoticed and provide a “second set of eyes”. False alarms would need to be low though; too many false positive alerts is a recipe for clinicians to lose trust in the system. In our these results, the precision for some conditions were low and associated with many false positives. This illustrates the need for further refinements so these alerts are more specific. Overall, we have demonstrated proof of principle that the current model achieves accuracy and error rates for multi-label ECG classification with traditional and deep features combined, but the system is not yet clinically useful. There is much room for improvement, especially where it comes to improving sensitivity for critical arrhythmias and reducing false positives before such a model could meaningfully decrease

either missed events or false alarms in the context of cardiac monitoring. Improvements such as more complete and reliable data, adding additional leads or patient data, or using more sophisticated architectures (i.e. transformer or attention models appropriate for the 12-lead ECG), may be the key to attaining the accuracy needed for clinically meaningful use.

VII. CONCLUSION

This study presented and compared three different methods for multi-label classification of 12-lead ECG records. As a starting point, we applied a methodology using conventional signal processing and extensive feature extraction with a shallow gradient-boosted trees ensemble. Second, we built a deep “beat-to-sequence” autoencoder model to autonomously learn features from raw ECG signals and used its embeddings within an MLP classifier. Lastly, we experimented with a hybrid approach, where deep autoencoder features were integrated with manually extracted features in an ensemble of gradient-boosted trees (with label-specific feature selection). The experimental evaluation addressed the hypotheses from the introduction. We confirmed Hypothesis 1: the classic feature-based ensemble performed better than the purely deep learning approach in terms of the Challenge metric and F-measure, supporting our expectation that a thoughtfully designed shallow model can rival or beat a deep neural network in this setting. We partially confirmed Hypothesis 2: prioritizing regularization of the feature inputs – through pruning and selecting the most informative features – was more beneficial than simply adding more features from the autoencoder without selection. In other words, judicious feature selection improved the Challenge score more than the naive inclusion of additional deep features. We did not find support for Hypothesis 3: combining deep autoencoder-derived features with the handcrafted feature set did not produce a statistically significant increase in classification performance. Despite the intuitive appeal of enriching the feature space with unsupervised learned features, our best results were achieved by the hybrid model with label wise top-1000 feature selection of autoencoder embeddings – and even that was on par with, not significantly above, the purely manual feature model. This winning configuration attained an average Challenge score of 0.4366 and an overall accuracy of $\sim 30.7\%$ on our test splits. These figures, while modest in absolute terms, were the highest in our comparisons. They highlight that combining traditional ECG features with modern machine learning can yield competitive results, but also that the deep features did

not offer a breakthrough improvement given our approach. In conclusion, our work illustrates both the potential and the challenges of multi-label 12-lead ECG classification: with careful feature design and model tuning, a relatively interpretable model (boosted trees on engineered features) can perform on par with a deep learning model, and a fusion of the two can work if feature selection is employed. However, the lack of a clear performance boost from the autoencoder features suggests that future deep learning efforts need to capture information complementary to what traditional features provide. We believe that incorporating more advanced deep architectures (e.g., 12-lead convolutional or transformer networks) and improving data quality will be important steps forward. The metrics achieved here set a baseline, but are not yet at a level for clinical adoption – bridging that gap will require both algorithmic innovations and perhaps new forms of model validation focusing on clinical relevance (e.g., reducing critical arrhythmia misses and alarm fatigue).

VIII. FUTURE WORK

There are multiple valuable avenues for further research to develop this work. One main focus is improving and augmenting the dataset. As we observed, the current training dataset is impacted by label uncertainty and other issues. Taking measures to clean the dataset - e.g., fixing mislabelled records, excluding excessively noisy ECG records, if any, ensuring labellers adhere to a well-defined set of labelling criteria - would likely improve model performance significantly. Furthermore, adding more data, particularly for under-represented arrhythmias, and/or utilizing data augmentation techniques, may similarly improve the generalization of deep learning models to previously unseen cases.

Another avenue that would be most valuable to explore would be assessing other lead arrangements and modalities. For instance, the dataset from the PhysioNet/CinC 2020 Challenge used 12-lead ECGs, but the 2021 Challenge was based on 2-lead recordings. The exploration of the features-based and hybrid models with minimizing number of leads would provide information on the robustness of the models, and potentially lead to modifications to the models, such as features that are most relevant to specific leads. On the other hand, the incorporation of some additional sources of complementary information, such as demographics of patients or symptoms, could provide additional context to the model - e.g., some arrhythmias are seen more commonly with older patients, or patients who have certain risk factors.

On the modelling side, cutting-edge deep learning techniques for time series hold strong potential. Transformer-based architectures, in particular, have shown great success at capturing long-range dependencies in sequential data. Recent studies, such as work by Natarajan et al., have demonstrated that “wide and deep” transformer models can process raw 12-lead ECG waveforms alongside derived features to achieve state-of-the-art arrhythmia classification. Extending these transformer approaches to our multi-label task – perhaps combined with the expert features we developed – is a natural next step. Such models might uncover subtle waveform patterns or lead interactions that our autoencoder or manually engineered features missed.

To conclude, expanding the classification paradigm to a larger set of ECG findings would improve the clinical utility of the model. Our work, like the referenced challenge, was limited to 27 diagnoses but real-life ECG interpretation requires the consideration of a....future work could try to train a more comprehensive multi-label model that consisted of additional arrhythmias and ECG abnormalities (e.g., more subtle ST/T changes, patterns of hypertrophy, etc.). While this would create new challenges (e.g., larger number of classes, extreme imbalance in the data), any success in this domain would propel us closer to achieving the concept of an AI generalist assistant for ECG interpretation. In conclusion, the follow-up steps are performed in parallel: improvements in data, experimenting with more advanced deep learning architectures (while maintaining interpretability), and incorporating more diagnostic categories into the model's training - all in the interest of establishing some degree of reliability and clinical meaningfulness of an ECG classifier.

Conflict of Interest

There is no conflict to declare.

Acknowledgement

The author would like to acknowledge the Department of Computer Science at Wichita State University for its support and resources that contributed to the successful completion of this research.

REFERENCES

- [1] S. S. Virani, A. Alonso, E. J. Benjamin, M. S. Bittencourt, C. W. Callaway, A. P. Carson, A. M. Chamberlain, A. R. Chang, S. Cheng, F. N. Delling, L. Djousse, M. S. Elkind, J. F. Ferguson, M. Fornage, S. S. Khan, B. M. Kissela, K. L. Knutson, T. W.

- Kwan, D. T. Lackland, T. T. Lewis, J. H. Lichtman, C. T. Longenecker, M. S. Loop, P. L. Lutsey, S. S. Martin, K. Matsushita, A. E. Moran, M. E. Mussolino, A. M. Perak, W. D. Rosamond, G. A. Roth, U. K. Sampson, G. M. Satou, E. B. Schroeder, S. H. Shah, C. M. Shay, N. L. Spartano, A. Stokes, D. L. Tirschwell, L. B. VanWagner, and C. W. Tsao, "Heart disease and stroke statistics update: A report from the American Heart Association," *Circulation*, vol. 141, no. 9, pp. e139–e596, 2020. <https://www.ahajournals.org/doi/abs/10.1161/CIR.0000000000000757>
- [2] H. Smulyan, "The computerized ECG: friend and foe," *The American Journal of Medicine*, vol. 132, no. 2, pp. 153–160, 2019. <http://www.sciencedirect.com/science/article/pii/S002934318308532>
- [3] R. O. Bonow, D. L. Mann, D. P. Zipes, and P. Libby, *Braunwald's Heart Disease: A Textbook of Cardiovascular Medicine*. Elsevier Health Sciences, 2011.
- [4] C. Breen, G. Kelly, and W. Kernohan, "ECG interpretation skill acquisition: A review of learning, teaching and assessment," *Journal of Electrocardiology*, 2019. <http://www.sciencedirect.com/science/article/pii/S0022073618306411>
- [5] AliveCor. AliveCor KardiaMobile & KardiaMobile 6L. <https://www.alivecor.com/> (Accessed November 4, 2020). <https://www.alivecor.com/>
- [6] Apple. Apple Watch. <https://www.apple.com/ca/watch/> (Accessed November 4, 2020). <https://www.apple.com/ca/watch/>
- [7] QardioMD. QardioMD: Wireless ECG Monitoring with QardioCore. <https://www.getqardio.com/en/qardiomd-ecg/> (Accessed November 4, 2020). [Online]. Available: <https://www.getqardio.com/en/qardiomd-ecg/>
- [8] General Electric Healthcare – Diagnostic ECG. <https://www.gehealthcare.com/products/diagnostic-ecg> (Accessed November 4, 2020). <https://www.gehealthcare.com/products/diagnostic-ecg>
- [9] Koninklijke Philips – Diagnostic ECG. <https://www.usa.philips.com/healthcare/solutions/diagnostic-ecg/diagnostic-ecg> (Accessed November 4, 2020). <https://www.usa.philips.com/healthcare/solutions/diagnostic-ecg/diagnostic-ecg>
- [10] Kligfield Paul, Gettes Leonard S., Bailey James J., Childers Rory, Deal Barbara J., Hancock E. William, van Herpen Gerard, Kors Jan A., Macfarlane Peter, Mirvis David M., Pahlm Olle, Rautaharju Pentti, and Wagner Galen S., "Recommendations for the Standardization and Interpretation of the Electrocardiogram," *Journal of the American College of Cardiology*, vol. 49, no. 10, pp. 1109–1127, Mar. 2007, publisher: American College of Cardiology Foundation. <https://www.jacc.org/doi/full/10.1016/j.jacc.2007.01.024>
- [11] E. A. Perez Alday, A. Gu, A. Shah, C. Robichaux, A.-K. I. Wong, C. Liu, F. Liu, A. B. Rad, A. Elola, S. Seyed, Q. Li, A. Sharma, G. D. Clifford, and M. A. Reyna, "Classification of 12-lead ECGs: the PhysioNet/Computing in Cardiology Challenge 2020," *Physiological Measurement*, 2020, In Press.
- [12] T. Chen and C. Guestrin, "XGBoost: A scalable tree boosting system," in *Proceedings of the 22nd ACM SIGKDD International Conference on Knowledge Discovery and Data Mining*, ser. KDD '16. New York, NY, USA: Association for Computing Machinery, 2016, pp. 785–794.
- [13] R. K. Vinayak and R. Gilad-Bachrach, "DART: Dropouts meet Multiple Additive Regression Trees," in *Proceedings of the 18th International Conference on Artificial Intelligence and Statistics (AISTATS)*. PMLR, Feb. 2015, pp. 489–497. <http://proceedings.mlr.press/v38/korlakaivinayak15.html>
- [14] Y. Bengio. Deep learning challenges. CS-Can 2020. <https://cscan-infocan.ca/feature-on-homepage/watch-deep-learning-challenges-with-yoshua-bengio/> (Accessed Nov 3, 2020). <https://cscan-infocan.ca/feature-on-homepage/watch-deep-learning-challenges-with-yoshua-bengio/>
- [15] A. Natarajan, Y. Chang, S. Mariani, A. Rahman, G. Boverman, S. Vij, and J. Rubin, "A Wide and Deep Transformer Neural Network for 12-Lead ECG Classification," in *2020 Computing in Cardiology (CinC) Challenge*, 2020, pp. 1–4. <https://raw.githubusercontent.com/physionetchallenges/physionetchallenges.github.io/master/2020/papers/107.pdf>



Advancements in CPW-Fed Antennas: Review on Design Techniques and Performance Optimization for 5G and Beyond

Manish Kumar¹, Sandeep Kumar Singh^{1*}, Arvind Kumar Singh², Tripurari Sharan³

¹Department of EEC, Sharda University, Uttar Pradesh, India

²Department of Electrical Engineering, NERIST, Nirjuli, Arunachal Pradesh, India, 791109

³Department of ECE, NERIST, Nirjuli, Arunachal Pradesh, India, 791109

Received date: 15/05/2025, Acceptance date: 25/06/2025

DOI: <http://doi.org/10.63015/10s-2464.2.3>

**Corresponding Author: _sandeepsingh.ec@sharda.ac.in*

Abstract

This review comprehensively explores recent advancements in coplanar waveguide (CPW)-fed antenna design, with a particular focus on performance optimization techniques applicable to 5G and future 6G wireless systems. The study investigates a wide array of design methodologies including the integration of stubs, slots, strips, corner truncation, substrate engineering, defected ground structures (DGS), defected substrates, metamaterials (MTM), frequency-selective surfaces (FSS), conductor-backed (CB) configurations, modified ground structures (MGS), metal reflectors, and MIMO architectures. A detailed parametric comparison reveals how these approaches significantly enhance key antenna parameters such as impedance bandwidth (up to 181%), gain (up to 13.1 dBi), axial ratio bandwidth, miniaturization (up to 72.7% size reduction), polarization purity, and frequency agility across multiple bands. Applications span 5G/6G mobile, biomedical, IoT, satellite, CubeSat, and vehicular systems. In particular, techniques like MIMO and metamaterial integration deliver high port isolation (≥ 15 dB), ultra-wideband (UWB) support, and enhanced diversity performance. This work provides a roadmap for selecting optimal design combinations tailored to specific wireless standards and platforms. Future research is encouraged to explore reconfigurable structures, AI-driven design automation, transparent and sustainable materials, and energy-harvesting integration for next-generation intelligent antenna systems.

Keywords: DGS, CPW-fed, CB-CPW Antenna, CB-MTS, FSS, CPW-MIMO Antenna.

1. Introduction: Antennas constitute a fundamental component in wireless communication systems [1]. Over the past two decades, there has been a significant surge in the demand for compact, low-cost, flexible, and broadband antennas. However, integrating multiple antennas into a single mobile device remains a challenging task due to spatial limitations, thereby necessitating effective isolation between coexisting communication technologies. Microstrip patch antennas, widely recognized for their compactness, lightweight structure, cost-efficiency, and compatibility with integrated circuit technologies, have become increasingly relevant in modern communication systems. These antennas typically support single-mode linearly polarized (LP) waves, which are oriented either horizontally or vertically [2]. To address the limitations of LP antennas, circularly polarized (CP) antennas are being increasingly explored due to their ability to support independent data transmission and reception, mitigate multipath fading, enhance resilience in diverse environmental conditions, and improve polarization matching accuracy [3]. Several slotted patch configurations such as E, S, and H-shaped patches, dual-polarized Xi-shaped designs, and inverted L-shaped parasitic strips have been developed to improve CP antenna bandwidth in indoor wireless scenarios [4]. These designs are often adapted for fifth-generation (5G) millimeter-wave applications, supporting multiple frequency bands including Industrial, Scientific, and Medical (ISM) bands (2.4–2.485 GHz, 5.725–5.875 GHz), Wireless Local Area Network (WLAN), Worldwide Interoperability for Microwave Access (WiMAX), Bluetooth, Ultra High Frequency (UHF), and sub-6 GHz 5G bands [5]. To enhance CP antenna performance further, modifications involving parasitic elements and ground planes have also been explored. CP antennas are well-suited for Radio Frequency Identification (RFID) applications

due to their reliability and stable wireless links, with RFID technology offering advantages such as high data rates, extended range, robust security, and multi-band operability. Designing CP antenna with wide 3-dB axial-ratio bandwidths remains a persistent challenge due to their inherent size constraints [6–8]. Nonetheless, proximity feeding and other techniques have helped in achieving broadband CP antenna operation, particularly for WiMAX, WLAN, and ISM bands [9]. Moreover, CP antennas have found applications in narrowband microstrip designs on substrates like FR4 and PTFE, particularly for Dedicated Short-Range Communication (DSRC) at 5.9 GHz [10]. With the advent of advanced wireless technologies, CPW offers advantages such as low radiation loss, compactness, ease of integration with monolithic microwave integrated circuits (MMICs), and wide impedance bandwidth. These attributes are especially beneficial for compact, flexible, and high-frequency systems like 5G and 6G. Compact CPW-fed implantable antennas have been introduced for biomedical telemetry, particularly within the ISM bands of 2.45 GHz and 5.8 GHz [11–12]. Low-profile, wideband, circularly polarized CPW-fed antennas have also been proposed for biotelemetry and body-worn applications [13], while similar configurations are optimized for GNSS and RFID systems [14]. Other implementations include vehicle-mounted CP antennas that operate in upper GNSS bands (1.559–1.606 GHz) [15]. CubeSats represent a prominent area where CPW-fed printed monopole and meta surface antennas are leveraged for compact satellite communication systems [16], with additional advancements in the use of additively manufactured meta surface structures to enhance CP antenna performance in the X-band [17]. These solutions are particularly effective in inter-satellite and satellite-to-ground communication links [18]. For sub-6 GHz massive machine-type communications, asymmetric CPW-fed CP antennas have been

designed to ensure high radiation efficiency and miniaturization [19]. Moreover, optically transparent CPW antennas on glass substrates have gained traction for automotive and aesthetic integration [20]. In high-density antenna systems, mutual coupling is mitigated using strategies like defected ground structures (DGS), electromagnetic bandgap structures, and parasitic elements [21]. Novel CPW-fed antenna designs targeting wearable and super-wideband applications have been proposed, including integration with emblematic structures like the Mercedes-Benz logo, for ISM band operation within Wireless Body Area Networks (WBANs) [22]. For vehicular communication systems, a CPW-fed patch antenna designed to operate at 5.9 GHz has been developed for DSRC applications, contributing to improved safety communications [23]. Innovative antenna geometries such as Om (Om) and double-Damru shapes fabricated on low-cost FR-4 substrates support multiband operations across S, C, and Ku-bands, including 5G systems [24, 25]. Other techniques employ inverted L-shaped elements, modified ground planes, and metamaterial loading to ensure performance across a wide frequency spectrum including GSM, Wi-Fi, WiMAX, LTE, and Ultra-Wideband (UWB) [26, 27]. Antenna arrays with 1×2 radiating elements and integrated DGS have been utilized to support dual-band operations such as GPS, GSM, UMTS, Bluetooth, and WiMAX [28]. Similarly, compact crown-shaped CPW-fed antennas have been reported for C- and X-band communication [29]. Double-patch CPW configurations are also effective in enhancing gain and bandwidth, particularly in WLAN environments [30]. Compact broadband CPW antennas have been engineered with favorable features such as mechanical durability, rapid thermal dissipation, and low loss, making them well-suited for ISM, RFID, and WLAN systems [31]. DGS continues to play a vital role in improving gain and bandwidth across

multiple bands, notably WLAN, UWB, and WiMAX [32–34]. CPW-fed meta surface antennas, especially miniaturized ones, have been proposed for 5G [35] and UWB applications [36], while textile-based antennas are being considered for Wireless Personal Area Networks (WPAN) and biomedical use on flexible substrates [37, 38]. Finally, frequency-selective surface (FSS)-integrated CPW antenna arrays with high front-to-back ratios have been proposed for aerospace, IoT, and wideband applications [39–41]. To address interference challenges in UWB communication, antennas with band-notch characteristics have been designed, effectively suppressing WiMAX, WLAN, and satellite signal interference [42–45]. CPW-fed antennas have proven themselves to be suitable for several applications, including 5G, and have wide potential to be implemented to make 6G antennas by optimizing the antennas with different techniques and achieving the desired gain, directivity, efficiency, and bandwidth. The size of the antenna [47] can also be easily optimized to fit the desired platform and be used for a wide variety of applications. The CPW-fed patch antenna's bandwidth, Voltage Standing Wave Ratio (VSWR), gain, and radiation pattern can all be influenced by several design techniques. However, all these characteristics can be improved by carefully adjusting the substrate material, ground plane, and radiating stub, followed by some additional techniques like DGS, FSS, MTM, CB-CPW, CB-MTS CPW, and MIMO for improving gain, directivity, and efficiency, as well as antenna miniaturization for multiple applications, including 5 G. This article will undertake and optimize the following parametric studies with various design methodologies.

In the following, the article is presented in four sections. In section 2, comparative study and design techniques have been discussed. In section 3, comparative outcomes and in section 4, conclusion and future scope is given.

2. Comparative Study and Design Techniques:

The appropriate design techniques and the right antenna is crucial because it greatly influences the RF system's performance, including factors like bandwidth and communication range. Researchers have introduced numerous methods to enhance antenna bandwidth and gain while minimizing size. Various approaches can adjust key antenna parameters such as bandwidth, gain, directivity, efficiency, and impedance matching enabling their use in diverse applications like WLAN, Wi-Fi, WiMAX, ISM bands, C-band, X-band, Ku/Ka bands, and 5G networks. Additionally, these modifications allow antennas to operate across multiple frequency bands simultaneously, increasing their versatility.

2.1. Effect of adding stubs, slots, strips, cutting corners: Recent years have seen significant advancements in CP ultra-wideband antenna designs. Various techniques, such as corner-cutting, slot-loading, branch-line loading, and inverted L-shaped microstrip structures on FR4 substrates, enhance CP radiation in microstrip antennas. Annular ring slots and inverted microstrips improve impedance matching over wider frequencies, making them ideal for satellite and broadband applications [1]. To achieve right-hand (RHCP) and left-hand (LHCP) circular polarization, CPW-fed slot antennas with L-shaped strips and stubs are studied [2]. Modifications like parasitic strips and ground-plane adjustments further extend CP bandwidth [4]. Monopole antennas with square-ring slits achieve a 70% axial ratio (AR) bandwidth (2.62–5.42 GHz) [5]. This article presents a CPW-fed antenna design using various substrate materials and techniques, demonstrating tunable multi-band operation (3.3–10.1 GHz) with optimized $|S_{11}|$, IBW, and gain [6]. A compact CPW-fed antenna with slotted patch and stub-loaded DGS achieves super wideband performance (1.21–24.66 GHz) and 9.4 dB gain, making it suitable for microwave




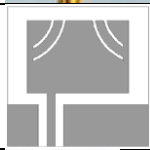
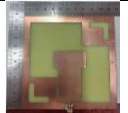

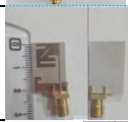
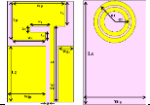
imaging applications [7]. For 5G, CPW-fed slot antennas with dual ground-plane slots enhance axial ratio and CP performance [8]. A compact asymmetric CPW-fed patch antenna with curved slits, designed on FR-4 substrate, achieves dual-band terahertz resonance at 0.813 THz and 1.254 THz with wide impedance bandwidths and high gain, making it suitable for 6G ultra-high-speed wireless communications [9]. Symmetrical L-shaped slits and widened tuning stubs enhance broadband CP operation [10]. Asymmetric ground planes and open slots improve mid/low-band AR and impedance matching [11]. Compact CPW-fed implantable antennas (2.45 GHz ISM band) use modified ground planes for wider bandwidth [12]. A miniaturized implantable CP antenna (3.4–7 GHz) is tested in human tissue [13]. CPW-fed inverted L-shaped monopoles with trimmed edges enhance IBW and ARBW [17]. Low-profile CP slot antennas cover multiple GNSS bands, with potential front-to-back ratio (FBR) improvement using reflectors [19]. Compact square-ring antennas with split corners achieve CP [20], while trapezoidal and L-shaped strips widen ARBW [21]. Triple-band CP antennas (2.4/3.5/5.8 GHz) use F-shaped feeds [22]. Transparent glass-substrate CP antennas maintain performance with mesh structures [23]. For ISM-band biotelemetry, CPW-fed antennas with etched slots ensure compact CP operation [24]. Narrowband microstrip patches on Polytetrafluoroethylene (PTFE)/ Flame Retardant Grade 4 (FR4) substrates suit 5.9 GHz DSRC [28]. Om-shaped [29] and U-shaped ground-plane antennas enable dual-band operation [31]. Square-shaped antennas with tunable stubs support multi-band applications [33]. The parametric analysis of incorporating stubs, slots, strips, and corner truncations, as discussed in [6] and summarized in Table 1, elucidates their collective impact on antenna performance.

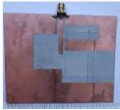
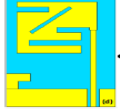
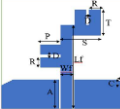
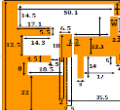
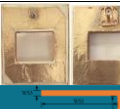

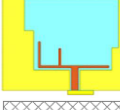
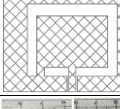
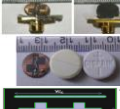



Scientific Impact: In CPW-fed antennas, integrating stubs, slots, strips, and corner cuts

offers powerful avenues to optimize electromagnetic behaviour:

- a) Stubs enable precise impedance matching, enhance bandwidth, and suppress harmonics, though at the cost of increased complexity.
- b) Slots in the radiator or ground plane facilitate antenna miniaturization, enable multi-band operation, enhance IBW, and allow polarization and pattern control, with minor trade-offs in radiation efficiency.
- c) Strips add tunable inductive or capacitive effects, improving impedance matching, coupling, and resonance tuning, while also assisting in multi-band and circular polarization performance.
- d) Corner cuts are crucial for generating circular polarization by exciting orthogonal modes with a 90° phase difference. They also influence impedance, and AR bandwidth, with slight gain reduction.

Table 1. Parametric effect of adding stubs, slots, strips, and cutting corners.

Design Technique	Antenna Layout	Antenna Area (mm ²)	Di-electric Substrate Material (ϵ_0)	IBW (-10dB GHz)	Gain (dBi)	Applications	Ref.
Stub with L-strip		18×18	FR4(4.4)	112%	4.2	Broadband, Satellite Communications	[2]
Slotted Patch Array		270×200	Air (1)	32.3%	9.0	Wi-Fi, WLAN	[3]
Slotted patch with DGS and stub		30 × 30	FR4(4.4)	181%	9.4	Microwave imaging (MI), SWB/UWB systems	[7]
Asymmetric CPW-fed curved slits		0.5 × 0.5	FR4(4.4)	11.4%, 23.4%	6.1, 7.3	6G terahertz communications, high-speed data links	[9]
Symmetrical Slits		116×116	FR4(4.4)	93.6%	3.4	UHF RFID	[10]
Asymmetric Ground		50×50	FR4(4.4)	103.5%	4.0	WLAN, Wi-MAX	[11]
Implanted Antenna		21×13.5	Rogers RT5880(2.2)	47.7%	15.8	ISM Band	[12]
Miniaturized CP		5×3	Polyimide substrate (2.78-3.48)	-	1.2	ISM Band	[13]

Rectangular Slots		88×89.9	Rogers RO3006(6.5)	129.5%	5	RFID, WLAN, Wi-MAX, GNSS	[14]
Etched Slot Patch		21×13.5	Flexible Roger RT5880(2.2)	47.7%	-	ISM Band	[15]
Inverted L-shaped		25×25	FR4(4.4)	13.4%	3.8	X- Band	[17]
Ground Slot, Reflector		70×70	Rogers RO3006(6.5)	28.4%	3.6	GNSS	[19]
Split Corner Patch		54×54	PVC (3-5)	19.0%	8-10	GNSS	[20]
L-shaped Strip		60×80	FR4(4.4)	100%	3.7	Sub -6GHz	[21]
Triple-Band Feed		63.5×55	-	-	4.8	Wi-Fi, Wi-Max, WLAN	[22]
Transparent CP		-	Glass (5-10)	28.6%	3.9	GPS L1 Band	[23]
Slot Etched Patch		9.5×2.3	Roger RT5880(2.2)	99.2%	15	ISM Band	[24]
Narrowband Patch		15×24.5	FR4(4.4)	-	1.8	DSRC	[28]
Om-Shaped Patch		80×80	FR4(4.4)	2%,2.3%, 2.9%,2%	2.2, 1.8, 11, 9.4	S-Band, IMT, C-Band, WI-MAX Band	[29]
Double Damru Shape		20×10	FR4(4.4)	1.1%,1.5, 1.4%,1.0%, 1.9%	2.7,5.1, 5.3, 4.5, 8.7	Ku Band, K-Band, 5G	[30]

2.2. Effect of Changes in the Substrate

Material: This approach examines various substrate materials and their key parameters, particularly focusing on dielectric properties, which critically influence the operational frequency range. A thicker substrate with a lower dielectric constant enhances radiation efficiency and widens the impedance bandwidth; however, it increases the antenna's physical dimensions. To address

this trade-off, high-permittivity substrates have been evaluated for Radio Frequency (RF) and microwave applications, enabling compact antenna designs while maintaining performance, as detailed in Table 2. The resonant frequency is determined by the substrate's area, thickness, and dielectric constant. Higher dielectric constants shift the fundamental resonance toward lower frequencies, especially when combined with

reduced substrate thickness. Consequently, high-permittivity materials facilitate antenna miniaturization without significantly compromising electrical performance [33].

Scientific Impact: The choice of substrate material in CPW-fed antennas plays a pivotal role in shaping electromagnetic performance, influencing parameters like miniaturization, bandwidth, efficiency, and fabrication ease. High-permittivity substrates such as Silicon, TMM 10i, and Duroid 6010 enable compact designs by lowering resonant frequencies, ideal for space-constrained RF/microwave systems, though often at the expense of radiation efficiency due to surface wave excitation. In contrast, low-permittivity

materials like Duroid 5880 and RO3700 deliver wider bandwidths and higher efficiency, trading off with larger physical sizes. Loss tangent is equally vital; low-loss substrates like Alumina and Duroid 5880 support high-gain and low-loss performance, while high-loss options like FR-4 degrade signal quality. From a manufacturing standpoint, soft substrates offer design flexibility but may introduce surface roughness and instability, whereas hard substrates ensure thermal durability and mechanical precision. Ultimately, achieving optimal antenna performance requires a careful balance of dielectric properties, mechanical traits, and application-specific needs.

Table 2: Properties of substrate materials

Substrate	Dielectric Permittivity at 10 GHz	Loss Tangent at 10 GHz ($10^4 \tan \delta$)	Surface Roughness (μm)	Thermal Conductivity ($\text{W/m}\cdot\text{K}$)	Dielectric Strength (kV/cm)	Soft or Hard Substrate
Alumina (Al_2O_3)	9.9	1–2	0.05–0.25	30–37	4000	Hard
Aluminum Nitride (AlN)	8.9	3–5	0.05–0.6	150–170	150	Hard
Glass (typical)	4–7	1	0.025	0.8–1.2	350	Hard
Silicon (Si)	11.9	10–100	<0.001	100–150	300	Hard
Duroid 5880	2.2	12	0.8–1.0	0.20	500	Soft
Duroid 6002	2.94	12	0.8–1.0	0.30	500	Soft
Duroid 6010	10.2–10.8	27	0.8–1.0	0.30	500	Soft
Duroid R/flex 3700	2.0	20	0.8–1.0	0.20	500	Soft
Duroid RO3003	3.0	13	0.8–1.0	0.50	500	Soft
Duroid RO3006	6.15	25	0.8–1.0	0.62	500	Soft
Duroid RO3010	10.2	35	0.8–1.0	0.62	500	Soft
Duroid RO4003	3.38	27	0.8–1.0	0.64	500	Soft
Duroid RO4350B	3.48	40	0.8–1.0	0.69	500	Soft
TMM 6	6.0	23	0.8–1.0	0.72	500	Soft
TMM 10	9.2	22	0.8–1.0	0.76	500	Soft
TMM 10i	9.8	20	0.8–1.0	0.76	1050	Soft



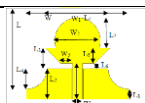
FR-4	4.5–4.8	220	~6	0.25	425–455	Soft
------	---------	-----	----	------	---------	------

2.3. Effect of using defected ground structure (DGS): A CPW-fed slot antenna incorporating a DGS is proposed [43] to improve gain for WLAN applications. The design employs vertical and horizontal DGS configurations, enhancing both gain and impedance bandwidth compared to conventional slot antennas. A dodecagram fractal broadband antenna is also presented, demonstrating multiband resonance, improved radiation patterns, and higher efficiency. The integration of DGS and feed slot further optimizes performance, suggesting potential refinements with alternative DGS geometries [51]. Another design features a tapered radiator with an embedded circular patch, operating at 4.45 GHz with reduced profile height. The DGS-implemented ground plane makes it suitable for wireless and biomedical devices [52]. Additionally, a T-shaped CPW-fed monopole antenna with staircase DGS achieves wide bandwidth, omnidirectional radiation, and stable gain, supporting Time Division-Synchronous Code Division Multiple Access (TD-SCDMA), Wideband Code Division

Multiple Access (WCDMA), LTE 33-41, Bluetooth, GPS, WLAN, and navigation systems [53]. Effects of using DGS parameters are summarized in Table 3.

Scientific Impact: Incorporating DGS into CPW-fed antennas offers a wealth of scientific benefits that elevate antenna performance. By introducing strategic defects in the ground plane, DGS enhances IBW, supporting wideband and UWB operations. It enables antenna miniaturization by increasing the electrical length without altering the physical size and serves as an effective harmonic suppressor, acting like a band-stop filter to eliminate unwanted frequencies. DGS also boosts radiation efficiency and gain by minimizing surface current losses, while offering superior control over current distribution, which aids in mode purity and polarization control, vital in circularly polarized and MIMO designs. Overall, DGS is a powerful technique for creating high-performance, compact, and adaptive CPW-fed antennas.

Table 3: Parametric effect of using defected ground structure

Design Technique	Antenna Layout	Antenna Area (mm ²)	Di-electric Substrate Material (ϵ_0)	IBW (-10dB GHz)	Gain (dBi)	Applications	Ref.
Circular patch with rectangular slot-loaded DGS		37 × 30	FR4(4.4)	90.9%	1.7–4.6	5G, C-band	[43]
Fractal DGS Patch		23×24	FR4(4.4)	111.0%	>1.5	WiMAX, WLAN, FCC band, C- and X-band.	[51]
Tapered Radiator		20×20	FR4(4.4)	-	2.5	UWB	[52]

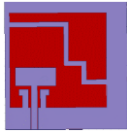


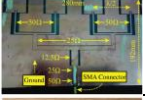

Staircase DGS Monopole		82×82	RT-Duroid (2.33)	84.0%	6.4	WLAN, CDMA, GPS, Wifi, Bluetooth, LTE.	[53]
------------------------	---	-------	------------------	-------	-----	--	------

Table 4: Parameters show the effect of using arrays

Design Technique	Antenna Layout	Antenna Area (mm ²)	Di-electric Substrate Material (ϵ_0)	IBW (-10dB GHz)	Gain (dBi)	Applications	Ref.
CPW-fed Array		-	FR4 (4.4)	6.0%	12.4	Aerospace	[36]
Wideband 2×2 CP Array		170×170	FR4 (4.4)	67.0%	6.0	UWB	[54]
Flexible CP Patch Array		280×192	(PET) substrate (1.8)	-	10.0	ISM	[55]
1×2 Array with DGS		170×105	Plexiglass substrate	20.0%, 74.0%	6.3	GPS, GSM, LTE, Bluetooth, Wi-Max, UTMS.	[35]

2.4. Effects of using arrays in radiation patch:

A compact CPW-slot line-fed CP microstrip array [36] demonstrates improved performance with a high front-to-back ratio. The design features simple geometries, low profile ($0.02\lambda_0$), and lightweight construction, achieving significant impedance bandwidth and 4.10% CP bandwidth while maintaining adequate gain. An alternative wideband CP array [54] employs sequential rotation feeding, showing enhanced performance in array configuration with better gain across the operational band and stable radiation characteristics. For biomedical applications, a flexible PET-based CPW-fed 2×2 patch array operates at 2.68 GHz with 10 dBi peak gain. The cost-effective design uses adhesive copper foils instead of traditional conductive inks, demonstrating good conformal performance and potential for wearable systems. Further optimization for ISM band applications is planned [55]. The designed 1×2 antenna array utilizes a Plexiglas substrate with defected ground structure


(DGS) implementation for enhanced bandwidth and impedance matching. The dual-band operation covers: 1.08-1.32 GHz (GPS band), 1.7-3.7 GHz (encompassing GSM, UMTS, Bluetooth, LTE, and WiMAX applications). A comprehensive parametric analysis of the DGS-modified ground plane revealed significant bandwidth improvement. The array demonstrates optimal radiation characteristics, including high efficiency and peak gain performance [35]. Key radiation patch array effects are summarized in Table 4.

Scientific Impact: Using arrays in the radiation patch of CPW-fed antennas enables a highly efficient, multi-functional, and application-tailored antenna design strategy. Scientific benefits include enhanced gain, wider bandwidth, CP improvement, and pattern control, making them suitable for advanced systems in aerospace, UWB, wearable tech, biomedical devices, and multiband wireless communications. When

combined with techniques like DGS and flexible substrates, these arrays offer next-

generation solutions for compact and high-performance antennas.

Table 5: Parameters showing the effect of using defected substrate

Design Technique	Antenna Layout	Antenna Area (mm ²)	Di-electric Substrate Material (ϵ_0)	IBW (-10dB GHz)	Gain (dBi)	Applications	Ref.
Defected Substrate Patch		42×36	FR4 (4.4)	100.0%	6.0	C and X Band	[37]

2.5. Effect of using defected substrate: A CPW-fed defected substrate microstrip antenna is proposed for wideband applications. Defected substrates also reduce the size of an antenna. The radiating patch of the proposed antenna is in the form of an extended U-shape. The space around the radiator is utilized by extending the ground plane on both sides of the radiator. The antenna has good return loss, constant group delay, and good radiation characteristics within the entire operating band. It has a maximum value of 88% and is applicable for C and X band applications [37]. Here is the effect of using defected substrate in Table 5.

Scientific Impact: Defected substrates offer a unique way to engineer antenna performance beyond traditional geometry tuning. By strategically modifying the substrate, designers can achieve miniaturization, wider bandwidth, higher efficiency, and better thermal stability.

2.6. Effect of using Notch band characteristics: A rectangular radiating patch is optimized to achieve an UWB response with an enhanced VSWR bandwidth of 11.88 GHz, while incorporating band-notched functionality at 3.5 GHz WiMAX without compromising radiation performance. Simulation results confirm its suitability for UWB applications with selective frequency rejection [25]. Further, compact CPW-fed UWB monopole



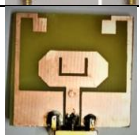

antennas are proposed, utilizing split ring slots (SRSs) for band-notched characteristics. The modified rectangular patch ensures wide impedance bandwidth across the UWB spectrum, while integrated SRS elements introduce rejection bands at 5.3 GHz WLAN and 7.4 GHz (X-band satellite communication). These designs are fabricated on low-cost FR4 substrates, maintaining a compact form factor [49]. The antenna uses a CPW feed, U-slot, split-ring resonators (SRRs), and mushroom-type EBG structures to achieve sharp notch characteristics [58]. Additionally, a CPW-fed UWB antenna with an inverted L-shaped structure demonstrates WLAN band rejection (5.15–5.85 GHz) while covering 3.02–11.34 GHz. Simulations align well with measurements, validating its performance [59]. The impact of notch band integration on antenna performance is summarized in Table 6.

Scientific Impact: Notch band integration in CPW-fed UWB antennas enables highly selective frequency rejection without compromising bandwidth, gain, or radiation performance. Using techniques like U-slots, SRRs, SRSs, and EBGs, designers can tailor the antenna response to suppress unwanted signals from coexisting services, making these antennas highly suitable for UWB communication, radar, and interference-prone environments. Combined with compact size, low-cost fabrication, and high

efficiency, these antennas represent a scientifically robust and practically viable

solution for next-generation wireless systems.

Table 6: Parameters showing the effect of using Notch band characteristics

Design Technique	Antenna Layout	Antenna Area (mm ²)	Di-electric Substrate Material (ϵ_0)	IBW (-10dB GHz)	Gain (dBi)	Applications	Ref.
U-slot, SRRs, EBGs		27×27	FR4(4.4)	147.0%	3.6-8.2	Wi-MAX, WLAN, X-Band	[25]
Split Ring Slot (SRS)		18×18	FR4(4.4)		8.8	UWB	[49]
U-slot, SRRs, and EBGs		25 × 25	FR4(4.4)	127.4%	1.2–3.9	UWB systems, interference rejection for C/X-band	[58]
Inverted L-slot		25×25	FR4(4.4)	47.4%, 58.6%	3	UWB	[59]

2.7. Effects of using metamaterial substrate: Digital light processing (DLP) and the micro-dispensing procedure for Rogers RadixTM and Nova Centrix HPS-FG57B conductive paste, respectively [18], are used in this work to additionally build the CPW-back-fed meta surface patch antenna. For wideband and polarization control, the meta surface is made up of truncated patches with designed sizes and relative arrangements. By using Rogers Radix, the substrate thickness could be optimized to achieve improved axial ratio, gain, and impedance bandwidth. For use with CubeSat applications, a wideband CP-printed dipole antenna with AMC is suggested [16]. Placing AMC at the back of the antennas improves the gain of the suggested antenna. The design includes a triangular cut at the upper edge of the right ground plane and asymmetric ground planes to achieve CP. The suggested printed monopole antenna has a wider 3dB ARBW and a greater gain while taking up less space in terms of physical dimensions. A metamaterial super-substrate-loaded concentric circle-shaped antenna with a coplanar waveguide [44] has been studied for

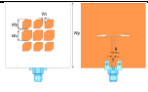
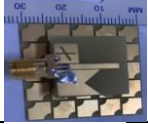
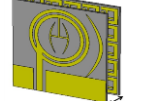

gain enhancement in three wideband modes. The proposed meta-surface's near-zero refractive index increases gain over a wide range of operations. It is more efficient and can be used for various applications, such as satellite communication, military, and medical monitoring. A resonator-based 3x3 metamaterial array [46] is used as a reflector plane below a wideband antenna to obtain optimal bandwidth and gain features. The antenna displays better outcomes and can be utilized in various satellite, wearable, and wireless applications. The proposed antenna has 2 to 16 GHz of total bandwidth and a peak gain of 13.1 dB. Table 7 shows the effect of using a metamaterial substrate.

Scientific Impact: The incorporation of metamaterial substrates in CPW-fed antennas enables a paradigm shift in antenna design, achieving high gain, ultra-wide bandwidth, polarization control, and compact, low-profile construction. With applications spanning CubeSats, X-band, WLAN, LTE-A, Wi-Fi, 5G, and UWB systems, MTM-enhanced antennas provide next-generation performance critical for advanced wireless, aerospace, and biomedical platforms. The

combination of engineered electromagnetic properties with innovative fabrication methods like DLP and additive printing

further strengthens their practical and scientific value.

Table 7: Parameters showing the effect of using a metamaterial substrate.

Design Technique	Antenna Layout	Antenna Area (mm ²)	Di-electric Substrate Material (ϵ_0)	IBW (-10dB GHz)	Gain (dBi)	Applications	Ref.
Additively Manufactured MTS		48.6×48.6	RogersRadix, NovaCentrix HPS-FG57B	63%	7.7	X-Band	[18]
CP Printed Dipole + AMC		6.2×6.2	FR4(4.4)	97.5%	7.3	X-Band, CubeSat	[16]
Concentric Circle + MTM		28×28	FR4(4.6)	42%, 22%, 47.5%	6.2	WLAN, LTE-A, 5G, Wi-Fi, and X-band	[44]
MTM Reflector (3×3 Unit)		14.8×14.8	FR4(4.4)	155%	13.1	UWB	[46]

2.8. Effects of using the frequency-selective surface technique in CPW: A novel miniaturized frequency-selective surface (FSS) design [34] is presented for CPW antenna gain enhancement, demonstrating a gain improvement from 1.8 dBi to 2.6 dBi while maintaining omnidirectional radiation. Optimal performance occurs at 2.45 GHz with scalable gain through FSS element multiplication, making it suitable for IoT, ground-penetrating radar, wireless communications, and medical imaging applications. A compact UWB antenna system incorporating a hexagonal patch with multiple stubs (5-17 GHz bandwidth) and a 5×5-unit cell FSS layer (9 mm spacing) achieves 15 GHz ultrawideband operation (3-18 GHz). This configuration demonstrates exceptional potential for 5G/6G applications due to its optimized size-volume-bandwidth-gain characteristics [39]. An aperture-coupled printed antenna [56] with dual-layer FSS reflectors (7×5 crossed elements) shows significant performance improvements: 63% bandwidth enhancement and 29.4%/15.8%

gain increase compared to single-layer implementations. The compact design features a bottom-substrate feed antenna and miniaturized unit cells, making it ideal for long-range communications. For UWB applications, a 50% miniaturized monopole antenna with 8×8 FSS reflector array achieves 2.55-13 GHz bandwidth (extended to 2.61-13 GHz with FSS) and stable 8.6 dBi peak gain. Experimental validation confirms ≥ 4 dBi gain improvement and enhanced lower-frequency bandwidth performance [57]. Table 8 summarizes the performance enhancements achieved through FSS integration in CPW antennas.

Scientific Impact: FSS integration transforms CPW-fed antennas into high-performance systems by combining filtering, gain enhancement, and bandwidth extension in a single compact structure. The choice of FSS geometry (crossed dipoles, hexagons, CSRRs) and layer configuration (single vs. dual) depends on the target frequency, gain, and application requirements. Through effective integration with stubs, patches, or

layered architectures, FSS transforms traditional CPW antennas into high-

performance, frequency-agile systems ready for modern wireless challenges.

Table 8: Parameters showing the effect of using a frequency-selective surface (FSS)

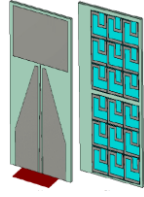


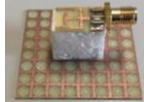
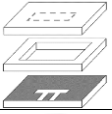
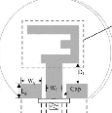
Design Technique	Antenna Layout	Antenna Area (mm ²)	Di-electric Substrate Material (ϵ_0)	IBW (-10dB GHz)	Gain (dBi)	Applications	Ref.
Miniaturized FSS		28.8×46.5	Upper substrate FR4(4.6) Lower substrate Rogers RT/duroid 5880(2.2)	62.5%	1.8-2.6	IoT	[34]
Stub-loaded Patch		50×50	Rogers RT/duroid 6002(2.94)	109%	10.5	UWB	[39]
Dual-layer FSS		30×32	FR4(4.4)	82.3%,44.5%	8.4	Long Distance Comm.	[56]
UWB FSS Reflector		40×40	FR4(4.4)	134%	8.6	UWB	[57]

Table 9: Parameters showing the effect of high permittivity substrates

Design Technique	Antenna Layout	Antenna Area (mm ²)	Di-electric Substrate Material (ϵ_0)	IBW (-10dB GHz)	Gain (dBi)	Applications	Ref.
High- ϵ_r Microstrip Design		-	Taconic CER-10	-	6.1	24GHz	[48]
Inverted E-shape Monopole		490	(Mg _{0.93} Zn _{0.07}) ₂ SnO ₄ microwave ceramic Substrate (8.5)	33.1%, 27.3%	4.4	ISM, HIPERLAN, UNII and WiMAX bands.	[50]

2.9. Effect of using high permittivity substrates: Two designs [48] of 24 GHz microstrip patch antennas using high-dielectric constant substrates have been presented, with high gain achieved using micromachining and superstrate. Multilayer construction and coplanar waveguides are used, with an air gap introduced to avoid surface waves. The new design uses the superstrate effect, and the measured gain value exceeds 6 dBi. Simulation and

measurement results are presented for two designs on high-permittivity substrates. A compact CPW-fed inverted-E-shaped monopole was successfully fabricated on a high-permittivity substrate. The antenna has a 10dB return loss and covers the ISM, Unlicensed National Information Infrastructure (UNII), High Performance Radio Local Area Network (HIPERLAN), and WiMAX bands. The monopole has a smaller size and comparable bandwidth

compared to the literature [50]. The effect of using high-permittivity substrates is shown in Table 9.

Scientific Impact: Using high-permittivity substrates in CPW-fed antennas facilitates size reduction, resonant frequency control, and gain enhancement, making them well-suited for compact, high-frequency, and multi-band applications. Through design techniques like micromachining, superstrate addition, and air-gap optimization, the traditional limitations of high- ϵ_r materials (e.g., bandwidth narrowing or surface wave excitation) can be effectively mitigated, allowing engineers to harness their full potential in ISM, 5G, satellite, and millimeter-wave systems.

2.10. Effects of using Conductor-backed CB-CPW antennas: A novel broadband monopole antenna design [41] has been engineered to achieve enhanced bandwidth characteristics while maintaining a compact form factor. The optimized structure demonstrates superior performance metrics including: High return loss (>15 dB), Extended operational bandwidth (covering ISM, RFID, and WLAN bands), Radiation efficiency exceeding 85%, Excellent thermal management properties. The design incorporates cost-effective manufacturing processes while offering: Minimal radiation losses (<0.5 dB), Robust mechanical durability, Aesthetic structural integrity, Simplified assembly procedures. A CPW (CB-CPW) broadband antenna design [42] has been developed for multi-beam operation in WLAN (5.15-5.25 GHz), RFID (5.8 GHz), and WiMAX applications. The innovative configuration features semi-circular ground

plane topology, Parasitic ground elements, Triple CPW feed structure. This architecture achieves broadband impedance matching ($VSWR < 2:1$), Enhanced thermal dissipation, Mechanical robustness. Experimental validation through prototype fabrication confirms the simulated performance characteristics. Table 10 quantitatively compares the performance enhancements achieved through CB-CPW implementation. P.S. Kumar et al [45] have proposed a miniaturized three-band antenna with a backed MTS. The triple frequency is created by combining the diamond-shaped patch with the (CB-MTS) CPW-fed antenna. The antenna covers the following 5G bands: 2.4–2.484 GHz for the IoT 3.6–4.2 GHz for the 5G mobile phone for satellite communication applications 5.35–5.47 GHz for the future of mobile broadband applications The proposed antenna has a 72.7% size reduction compared to a conventional rectangular patch. Table 10. shows the effect of using (CB-MTS) CPW antennas.

Scientific Impact: Using conductor-backed (CB) structures in CPW-fed antennas enables broadband operation, footprint reduction, thermal resilience, and high radiation efficiency. The combination of electromagnetic optimization and mechanical benefits makes CB-CPW antennas highly suitable for compact, low-cost, and high-performance wireless systems, including 5G, WLAN, RFID, IoT, and CubeSat platforms. Designs like CB-MTS further extend these advantages by adding multiband functionality and metasurface-enhanced gain, paving the way for next-generation miniaturized RF devices.

Table 10: Parameters showing the effect of using conductor-backed CB-CPW antennas

Design Technique	Antenna Layout	Antenna Area (mm ²)	Di-electric Substrate Material (ϵ_0)	IBW (-10dB GHz)	Gain (dBi)	Applications	Ref.
------------------	----------------	---------------------------------	---	-----------------	------------	--------------	------

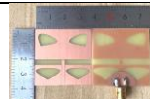


CB-CPW Monopole		38×38	FR4(4.4)	60%	3.3	ISM, RFID, WLAN	[41]
Triple CPW Feed Patch		40×40	FR4(4.4)	60%	3.9	WLAN, RFID, Wi-Max	[42]
CB-MTS Patch Antenna		22×23	FR4(4.4)	7.5%, 13.2%, 7.4%	3.6	5G	[45]

Table 11: Parameters showing the effect of using MGS, FSS, DGS, and MTM.


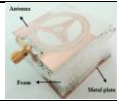

Design Technique	Antenna Layout	Antenna Area (mm ²)	Di-electric Substrate Material (ϵ_0)	IBW (-10db GHz)	Gain (dBi)	Applications	Ref.
MGS + FSS + DGS + MTM		17×20	FR4(4.4)	35.6%, 18%, 10.7%, 18.3%	--	GSM, Wi-Fi, WLAN, Wi-Max,	[32]

Table 12: Parameters showing the effect of using metal reflector plates.

Design Technique	Antenna Layout	Antenna Area (mm ²)	Di-electric Substrate Material (ϵ_0)	IBW (-10db GHz)	Gain (dBi)	Applications	Ref.
CPW-fed patch with reflector		35×35	Rogers 4003C (3.55)	15.1%	7.3	WBAN	[27]
Notch-banded CPW-fed patch with reflector		30×20	FR4(4.4)	11.0%, 4.3%, 43.4%	10.0	Bluetooth, WLAN, WI-MAX, UWB	[40]

2.11. Effect of using Modified Ground Structure (MGS) and Frequency Shifting Strips (FSS), along with Defected Ground Structure (DGS) and Metamaterial (MTM): An FR4-based CPW-fed multiband antenna with a 17×20mm diameter is designed with a modified ground structure, frequency shifting strip, defected ground structure, and metamaterial loading on the lower side of the antenna. This multiband antenna operates at 1.702 MHz, 3.202 MHz, 5.302 MHz, and 10.302 MHz, covering GSM 1800/900 MHz, Wi-Fi/WLAN (5.2/5.5 GHz), and WiMAX 3.3 GHz [32]. Table 13 shows

the effects of using MGS, FSS, DGS, and MTM.

Scientific Impact: Using MGS, FSS, DGS, and MTM in CPW-fed antennas results in a powerful compact, multiband, and broadband solution with controlled radiation and harmonic suppression. These techniques synergize to improve impedance bandwidth, enable multiband tuning, reduce antenna size, and optimize radiation characteristics, making them ideal for multi-standard wireless devices, including GSM, Wi-Fi, WLAN, and WiMAX. The compact design with frequency agility also ensures high

integration potential in portable, wearable, and smart IoT platforms.

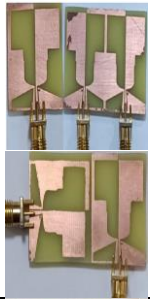


2.12. Effect of using metal reflector plates:

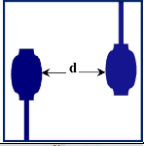
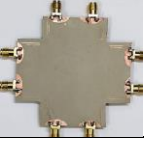
Mercedes-Benz has developed a modified logo with a CPW-fed antenna to control radiation towards the human body. A metal plate was used as a reflector to reduce human body loading on the antenna. The antenna performed well on the actual and modeled body and is suitable for WBAN communication systems [27]. Table 14. shows the effect of using metal reflector plates. K.G. Jangid et al [40] have described the design and performance of a UWB antenna with triple band notched features and increased gain. The proposed CPW-fed patch antenna has two U-shaped slots on the patch, an inverted U-shaped slot in the feed line, and a metallic reflector beneath the antenna structure. The three rejection bands were obtained by inserting three U-slots of varying sizes and locations into the radiator. The

antenna's maximum gain is close to 9.88 dBi at 7.4 GHz. This antenna is helpful for modern ultra-wideband communication systems, except for 3.5 GHz WIMAX, IEEE 802.11a/h/j/n WLAN, and ITU 8 GHz systems. Table 12 shows the effect of using metal reflector plates with notch bands.

Scientific Impact: Metal reflector plates in CPW-fed antennas significantly enhance performance by reducing SAR and enhancing safety in wearable devices, improving gain and directionality, enabling notch-band rejection for interference avoidance, and stabilizing radiation patterns in wideband and multi-band scenarios. This makes them highly effective for WBAN, Bluetooth, WLAN, WiMAX, and UWB applications, particularly where directional control and spectral cleanliness are essential.

Table 13: Parameters show the effect of using CPW-fed MIMO Antennas

Design Technique	Antenna Layout	Antenna Area (mm ²)	Di-electric Substrate Material (ϵ_0)	IBW (-10db GHz)	Gain (dBi)	Applications	Ref.
Modified F-shaped radiator Spatial Diversity, Pattern Diversity MIMO		24×22 (Single Element)	FR4(4.4)	173.3%	8.6	UWB, SWB	[38]
		24×43 (Spatial Diversity)	FR4(4.4)	174.2%			
		24×47 (Pattern Diversity)	FR4(4.4)	174.2%			
Octagonal slot, L-shaped stub, two element MIMO		38.4×20	FR4(4.4)	154.3%	8.9	5G, C-Band, K-Band, mm Wave	[26]
Hexagonal shaped patch, L-shaped grounded strips		40×40	Polyimide (3.5)	122.5%	6.3	UWB and X-Band Applications	[60]

Modified rectangular radiating element.		6×17.37	RO5880 (2.2)	15.1%	6.7	5G mm-wave applications	[61]
Key-type slotted-radiating patch		126.49×126.49	RO5880 (2.2)	165.7%	9.9	Multi-band applications	[62]

2.13. Effects of using MIMO CPW-fed antennas:

A quad-band circularly polarized monopole antenna [38] is presented for extended UWB applications, with a two-element MIMO configuration optimized for C-band, K-band, and mm-wave operation. Key performance characteristics include Peak gain of 6.73 dB, Radiation efficiency of 96%, impedance bandwidth of 3.7-29.27 GHz, four distinct CP bands with 3 dB axial ratio bandwidths of 35.5%, 1.5%, 4.6%, and 0.51%. The design incorporates modified U-shaped symmetrical decoupling structures in the MIMO configuration, achieving port isolation >16 dB across the operational bandwidth, suitable for C-band, Ku-band, 5G, Ka-band, mm-wave, and UWB applications [26]. A complementary quasi-complementary super-wideband antenna element (24 × 22 mm) demonstrates ultra-wide bandwidth of 3-42.1 GHz (173.3% fractional bandwidth), Modified F-shaped radiator with tapered CPW feed, Ground plane slot optimization, MIMO configuration (24 × 43 mm) maintains port isolation ≥15 dB, envelope correlation coefficient <0.008, operational range: 2.9-42.14 GHz [38]. This paper presents a compact 4-port CPW-fed flexible MIMO antenna, where the elements are arranged orthogonally to enhance isolation (> -17 dB) without additional decoupling structures. It demonstrates excellent diversity performance and stable operation under bending, making it ideal for wearable electronics [60]. This work proposes a two-port MIMO antenna with anti-parallel layout and defected ground structure (DGS) for mmWave 5G applications. The design eliminates the need for complex decoupling techniques and

ensures robust diversity performance [61]. This paper introduces an eight-port key-shaped MIMO antenna with an asymmetric feedline. The antenna exhibits stable performance under 45° bending and is well-suited for multi-band wireless systems [62]. Table 13 quantifies the performance enhancements achieved through CPW-fed MIMO antenna implementation.

Scientific Impact: MIMO integration in CPW-fed antennas transforms them into high-performance systems with ultra-wideband coverage, low mutual coupling & high isolation, enhanced gain and efficiency, compact and flexible configurations, suitability for UWB, 5G, mmWave, and wearable applications. These scientific enhancements make CPW-fed MIMO antennas indispensable in next-gen wireless platforms requiring speed, reliability, compactness, and multi-band diversity.

3. Comparative Outcomes: In this article, we review the various design techniques of CPW-fed antennas. Adding the stubs, slots, and strips method has miniaturized the size of the antenna for multi-band wireless applications [7,9]. The microwave soft substrate materials for microwave applications are usually used for CPW-fed patch antenna designs with different permittivities and thicknesses [12]. The thicker substrate offers more efficiency and a wider IBW for a lower dielectric constant, but a larger antenna. Hence, substrates with high dielectric constants favor small antenna sizes as compared to other conventional antennas [48, 49]. DGS offers significant gain

improvement over the entire band of operation compared to conventional slot antennas without DGS [53]. The number of arrays on the radiating patch also improves the gain of the antenna. [36, 55]. Using arrays with the DGS technique contributed to the bandwidth enhancement of the antenna with good efficiency and gain [35]. CPW-fed defected substrate microstrip antennas show a reduction in antenna size with wideband applications [37]. CPW-fed antennas with band-notch characteristics are used to enhance impedance bandwidth for the entire UWB frequency range and to generate band rejection at desired frequencies [25, 49]. Metamaterial arrays can be used as a reflector plane below the ground structure to obtain optimal bandwidth and gain features for UWB applications [46]. By using an FSS array containing subsequent unit cells, it improves the gain and bandwidth over the entire frequency range and is also offered for antenna miniaturization [39, 56, 57]. The CB-CPW band monopole antenna has been developed with various features to expand bandwidth and reduce size, be easy to process and assemble, have fast heat-dissipating speed, and have small radiation [41, 42].

4. Conclusion and Future Directions

(a) Research Contributions: This study comprehensively analyzes the impact of various design techniques like stubs, slots, DGS, FSS, metamaterials, and substrate modifications on CPW-fed antenna performance. Key contributions include:

1. **Bandwidth Enhancement:** Techniques like DGS and asymmetric ground planes achieve 181% IBW [7] and multi-band operation [6].
2. **Circular Polarization (CP):** L-shaped strips and corner truncations improve ARBW [10, 21].
3. **Miniaturization:** High-permittivity substrates (e.g., RO3010) and defected structures reduce size while maintaining performance [37, 48].

4. **Interference Mitigation:** Notch bands (e.g. U-slots, SRRs [58]) reject WLAN/WiMAX frequencies without compromising UWB operation.

5. **Gain and Efficiency:** Metamaterial substrates [16] and FSS reflectors [34] boost gain up to 13.1 dBi.

(b) 5G and Beyond Applications

1. **Sub-6 GHz and mm Wave:** Compact designs [26, 61] support 5G bands (3.5 GHz, 28 GHz) with MIMO configurations.
2. **6G Terahertz:** Curved-slit antennas [9] enable dual-band THz operation (0.813/1.254 THz) for ultra-high-speed communications.
3. **IoT/Wearables:** Flexible arrays [55] and implantable antennas [12] cater to biomedical and conformal applications.

(c) Research Gaps and Future Directions

1. **Reconfigurability:** Limited work on tunable notch bands using varactors/MEMS for dynamic spectrum adaptation.
2. **AI-Driven Design:** Machine learning could optimize stub/slot placement for enhanced CP and bandwidth.
3. **Energy Efficiency:** Integration with RF energy harvesting for self-powered IoT devices.
4. **THz and Optical Antennas:** Further exploration of transparent antennas [23] and plasmonic structures for 6G.
5. **MIMO Scalability:** Decoupling techniques for high-density MIMO arrays in mm Wave systems.

Motivation and Outlook

The demand for compact, multi-band, and high-gain antennas drives innovation in CPW-fed designs. Future work should focus on:

1. **Multi-functional Integration:** Combining sensing, energy harvesting, and communication in a single antenna.

2. **Sustainable Materials:** Eco-friendly substrates with low loss for green wireless systems.
3. **Standardization:** Benchmarking performance metrics for 5G/6G and industrial IoT applications.

This study bridges theoretical advancements with practical applications, paving the way for next-generation wireless systems.

Conflict of Interest: The Authors declare no conflicts of interest.

Acknowledgment: The authors gratefully acknowledge the unwavering support and encouragement provided by the Department of EECE, Sharda University, which has been instrumental in the successful completion of this research.

5. References:

- [1] Z.-H. Ma et al., Design of planar microstrip Ultrawideband circularly polarized antenna loaded by annular-ring slot, *International Journal of Antennas and Propagation*, 2021, pp. 1–10.
- [2] S. Patil, A.K. Pandey, and V.K. Pandey, A compact, wideband, dual polarized CPW-fed asymmetric slot antenna for wireless systems, *Journal of Microwaves, Optoelectronics and Electromagnetic Applications*, 19(3), 2020, pp. 343–355.
- [3] K.L. Chung et al., Circularly-polarized linear antenna array of non-identical radiating patch elements for WIFI/WLAN applications, *AEU - International Journal of Electronics and Communications*, 129, 2021, p. 153526.
- [4] U. Ullah and S. Koziel, A geometrically simple compact wideband circularly polarized antenna, *IEEE Antennas and Wireless Propagation Letters*, 18(6), 2019, pp. 1179–1183.
- [5] S.K. Singh, T. Sharan, and A.K. Singh, Enhancing the axial ratio bandwidth of circularly polarized open ground slot CPW-fed antenna for Multiband Wireless Communications, *Engineered Science*, 2021.
- [6] M. Kumar, Y. D. Banda, F. W. Aldbea, S. V. Savilov, S. K. Singh et al., Investigation of substrate materials laminated CPW-Fed patch antennas: Opportunities and challenges, *CNS&E Journal*, 1(3), May 2024, pp. 211–220.
- [7] M. Sekhar, N. Suman et al., CPW Fed Super-Wideband Antenna for Microwave Imaging Application, *Progress in Electromagnetics Research C*, 130, 2023, 201–212.
- [8] S.F. Seyyedrezaei et al., A novel small size CPW-fed slot antenna with circular polarization for 5G application, *Progress in Electromagnetics Research C*, 106, 2020, pp. 229–238.
- [9] K. K. Naik et al., Asymmetric CPW-fed patch antenna with slits at terahertz applications for 6G wireless communications, *Wireless Networks*, 30(6), 2024, 2343–2351.
- [10] R. Ma and Q. Feng, Design of broadband circularly polarized square slot antenna for UHF RFID applications, *Progress in Electromagnetics Research C*, 111, 2021, pp. 97–108.
- [11] Q. Fu, Q. Feng and H. Chen, Design and optimization of CPW-fed broadband circularly polarized antenna for multiple communication systems, *Progress in Electromagnetics Research Letters*, 99, 2021, 65–74.
- [12] A.D. Butt et al., Single-fed broadband CPW-fed circularly polarized implantable antenna for sensing medical applications, *PLOS ONE*, 18(4), 2023.
- [13] S. Ahmad et al., A compact wideband flexible circularly polarized

- implantable antenna for biotelemetry applications, 2021 IEEE International Symposium on Antennas and Propagation and USNC-URSI Radio Science Meeting (APS/URSI), 2021.
- [14] A. Gharaati et al., A low-profile wideband circularly polarized CPW slot antenna, *AEU - International Journal of Electronics and Communications*, 129, 2021, 153534.
- [15] S. Ahmad et al., A low-profile CPW-fed circularly polarized antenna for biomedical applications, 2022 IEEE International Symposium on Antennas and Propagation and USNC-URSI Radio Science Meeting (AP-S/URSI), 2022.
- [16] M.E. Hammoumi et al., A wideband circularly polarized CPW-fed printed monopole X-band antenna for CubeSat Applications, *IEEE Access*, 11, 2023, 121077–121086.
- [17] R. Tripathy, K. Sumana, and S.R. Patre, A low-profile UNIPLANAR circularly polarized monopole antenna for X-band applications, 2022 IEEE 9th Uttar Pradesh Section International Conference on Electrical, Electronics and Computer Engineering (UPCON), 2022.
- [18] J. O’Keefe et al., An additively manufactured CPW-back-fed wideband circularly-polarized radix metasurface patch antenna for X-band space applications, 2023 IEEE International Conference on Wireless for Space and Extreme Environments (WiSEE), 2023.
- [19] A. Gharaati, A. Goudarzi, and R. Mirzavand, compact circularly polarized CPW-fed antenna for GNSS applications, 2021 IEEE International Symposium on Antennas and Propagation and USNC-URSI Radio Science Meeting (APS/URSI), 2021.
- [20] A. Nikam and R. Patil, Design of circularly polarized antenna for vehicular GNSS application, 2023 Second International Conference on Electrical, Electronics, Information and Communication Technologies (ICEEICT), 2023.
- [21] B. Qiu and Y. Li, Asymmetric CPW-fed wideband circularly polarized antenna for sub-6 GHz application, 2020 IEEE 3rd International Conference on Electronic Information and Communication Technology (ICEICT), 2020.
- [22] N. K. et al., Time variant circularly polarized CPW antenna for WIFI/ISM/wi-max/wi-lan communication applications, 2023 IEEE Wireless Antenna and Microwave Symposium (WAMS), 2023.
- [23] W. Zhong and Y.-X. Sun, Wideband circularly polarized antenna on glass substrate with high optical transparency, 2022 International Symposium on Antennas and Propagation (ISAP), 2022.
- [24] V. Kaim et al., Ultra-miniature circularly polarized CPW-fed implantable antenna design and its validation for biotelemetry applications, *Scientific Reports*, 10(1), 2020.
- [25] K. Kaur, A. Kumar and N. Sharma, A novel design of ultra-wideband CPW-fed printed monopole antenna for Wi-MAX, WLAN and X-band rejection characteristics, *Analog Integrated Circuits and Signal Processing*, 114(1), 2023.
- [26] R. Mali, D. Lodhi and S. Singhal, Quad broadband circularly polarized CPW FED cleaver-shaped extended UWB MIMO antenna for 5G, C, K and millimetre wave applications, *Analog Integrated Circuits and Signal Processing*, 2023.
- [27] S. Kiani, P. Rezaei and M. Fakhr, A CPW-fed wearable antenna at ISM band for biomedical and WBAN

- applications, *Wireless Networks*, 27(1), 2021, 735–745.
- [28] M.Y. Sai et al., CPW Fed Microstrip Patch Antenna for Dedicated Short-Range Communication, *Wireless Personal Communications*, 122(4), 2021, 3859–3873.
- [29] A.Kr. Yadav et al., Design and Analysis of CPW-Fed Antenna for Quad-Band Wireless Applications, *Journal of Electronic Materials*, 52(7), 2023, 4388–4399.
- [30] A.Kr. Yadav, S. Lata and S.Kr. Singh, Design and Investigation of a Double-Damru (Pellet Drum)-Shaped CPW-Fed Microstrip Patch Antenna for 5G Wireless Communications, *Journal of Electronic Materials*, 52(7), 2023, 4400–4412.
- [31] Md. M. Alam et al., A dual-band CPW-fed miniature planar antenna for S-, C-, WiMAX, WLAN, UWB, and X-band applications, *Scientific Reports*, 12(1), 2022.
- [32] J. Borah et al., Miniaturization and Optimization of FR4-Based CPW-fed Antenna for Multiband Applications, *Radio Electronics and Communications Systems*, 64(12), 2021, 660–668.
- [33] S.K. Singh, T. Sharan and A.K. Singh, Investigating the S-parameter ($|S_{11}|$) of CPW-fed antenna using four different dielectric substrate materials for RF multiband applications, *AIMS Electronics and Electrical Engineering*, 6(3), 2022, 198–222.
- [34] S.N. Azemi et al., Gain Enhancement of CPW Antenna for IoT Applications using FSS with Miniaturized Unit Cell, *Journal of Physics: Conference Series*, 1962(1), 2021, 012052.
- [35] C. Ben Nsir et al., Design of a 1×2 CPW Fractal Antenna Array on Plexiglas Substrate with Defected Ground Plane for Telecommunication Applications, *Engineering, Technology & Applied Science Research*, 11(6), 2021, 7897–7903.
- [36] Y. Liu and K. Huang, CPW-fed circularly-polarized antenna array with high front-to-back ratio and low-profile, *Open Physics*, 16(1), 2018, 651–655.
- [37] A. Sharma et al., Design of CPW-Fed Antenna with Defected Substrate for Wideband Applications, *Journal of Electrical and Computer Engineering*, 2016, pp. 1–10.
- [38] D. Lodhi and S. Singhal, CPW-fed quasi-complementary super-wideband MIMO antenna, *Optical and Quantum Electronics*, 54(12), 2022.
- [39] M. Hussain et al., Bandwidth and Gain Enhancement of a CPW Antenna Using Frequency Selective Surface for UWB Applications, *Micromachines*, 14(3), 2023, p. 591.
- [40] K.G. Jangid et al., Triple-Notched Band CPW fed UWB Antenna with Metallic Reflector for High Gain Performance, *Advanced Electromagnetics*, 6(4), 2017, 15–21.
- [41] Z. Ding et al., A Novel Broadband Monopole Antenna with T-Slot, CB-CPW, Parasitic Stripe and Heart-Shaped Slice for 5G Applications, *Sensors*, 20(24), 2020, p. 7002.
- [42] Z. Ding, D. Zhang and C. Ma, Broadband Antenna Design with Integrated CB-CPW and Parasitic Patch Structure for WLAN, RFID, WiMAX, and 5G Applications, *IEEE Access*, 8, 2020, 42877–42883.
- [43] M. F. M. Omar, A. A. Manaf, M. F. Ain, S. K. A. Rahim et al., CPW-fed circular patch antenna with rectangular slot-loaded DGS for wideband application, *ELEKTRIKA*, 24(1), 2025, 7–13.
- [44] A.S. Priyadharshini, C. Arvind and M. Karthikeyan, Novel eng metamaterial for gain enhancement of an offset fed CPW concentric circle shaped patch antenna, *Wireless*

- Personal Communications, 130(4), 2023, 2515–2530.
- [45] P.S. Kumar and B.C. Mohan, Design of a miniaturized triple-band antenna with conductor-backed metasurfaces-CPW fed for 5G wireless applications, 2017 IEEE International Conference on Antenna Innovations & Modern Technologies for Ground, Aircraft and Satellite Applications (iAIM), 2017.
- [46] D. Negi and R. Khanna, A high-gain CPW-fed metamaterial antenna for UWB applications, Progress in Electromagnetics Research C, 132, 2023, 51–63.
- [47] M.F. Saad et al., CPW-UWB flexible composite antenna using jute textile for WPAN applications, 2020 IEEE International RF and Microwave Conference (RFM), 2020.
- [48] S. Aditya et al., High-gain 24-GHz CPW-fed microstrip patch antennas on high-permittivity substrates, IEEE Antennas and Wireless Propagation Letters, 3, 2004, 30–33.
- [49] K. Kaur, A. Kumar and N. Sharma, Split ring slot loaded compact CPW-fed printed monopole antennas for ultra-wideband applications with band Notch Characteristics, Progress in Electromagnetics Research C, 110, 2021, 39–54.
- [50] Y. Chen and C. Hsu, Inverted-E shaped monopole on high-permittivity substrate for application in industrial, scientific, medical, high-Performance Radio Local Area Network, unlicensed national information infrastructure, and worldwide interoperability for Microwave Access, IET Microwaves, Antennas & Propagation, 8(4), 2014, 272–277.
- [51] R. Teotia and T. Shanmuganantham, CPW-fed dodecagram fractal antenna with DGS for Multiband Applications, 2015 IEEE International Conference on Signal Processing, Informatics, Communication and Energy Systems (SPICES), 2015.
- [52] J. Gandhimohan and T. Shanmuganantham, CPW fed bud shaped antenna with DGS in UWB range for body area network, 2017 IEEE International Conference on Antenna Innovations and Modern Technologies for Ground, Aircraft and Satellite Applications (iAIM), 2017.
- [53] M. Dixit and M.G.S. Tripathi, CPW-fed monopole printed antenna using staircase shaped defected ground structure for wireless application, 2018 IEEE International Students' Conference on Electrical, Electronics and Computer Science (SCEECs), 2018.
- [54] M. Nosrati and N. Tavassolian, A wideband, high-gain, CPW-fed, circularly-polarized, L-shaped slot antenna array, 2017 IEEE International Symposium on Antennas and Propagation and USNC/URSI National Radio Science Meeting, 2017.
- [55] U. Farooq et al., Design of a 1×4 CPW microstrip antenna array on PET substrate for biomedical applications, 2019 IEEE International Symposium on Antennas and Propagation and USNC-URSI Radio Science Meeting, 2019.
- [56] H. Paik et al., High performance CPW fed printed antenna with double layered frequency selective surface reflector for bandwidth and gain improvement, Progress in Electromagnetics Research Letters, 102, 2022, 47–55.
- [57] W. Abbas Awan et al., A Frequency Selective Surface Loaded UWB Antenna for High Gain Applications, Computers, Materials & Continua, 73(3), 2022, 6169–6180.
- [58] G. Kumar, D. Singh, R. Kumar et al., A planar CPW fed UWB antenna with dual rectangular notch band

- characteristics incorporating U-slot, SRRs, and EBGs, *International Journal of RF and Microwave Computer-Aided Engineering*, 31(4), 2021, e22676.
- [59] A.S. Fazal et al., A compact UWB CPW-fed antenna with inverted L-shaped slot for WLAN band notched characteristics, 2017 11th European Conference on Antennas and Propagation (EUCAP), 2017.
- [60] G. Rajesh, R. Poonkuzhali, Design and analysis of CPW fed ultrathin flexible MIMO antenna for UWB and X-band applications, *IEEE Access*, 12, 2024, 96704–96713.
- [61] O. Elalaouy, M. EL Ghzaoui, J. Foshi, A high-isolated wideband two-port MIMO antenna for 5G millimeter-wave applications, *Results in Engineering*, 23, 2024, 102466.
- [62] S. Naik, A. Upmanyu, M. Sharma, Design and experimental analysis of asymmetric fed key-shaped eight-port flexible frequency diversity MIMO antenna with multi-band applications, *Optical and Quantum Electronics*, 57, 2025, 98.

News & Views

The Impact of Stress on Education: Understanding the Consequences and Finding Solutions

Rooma Pathak

M M Public School, Vasudha Enclave, Pitampura Delhi-110034

DOI: <http://doi.org/10.63015/NW-2501.2.3>

Author mail: roomasharda@gmail.com

Stress and education are intricately linked, with the pressure to perform well academically often taking a toll on students' mental and emotional well-being. Chronic stress can have severe consequences on students' cognitive, emotional, and social development, ultimately affecting their academic achievement and overall quality of life.

Causes of Stress in Education

1. Academic Pressure: High expectations from parents, teachers, and peers can create undue stress.
2. Excessive Homework: Overwhelming assignments and deadlines can lead to burnout.
3. Standardized Testing: High-stakes exams can cause anxiety and stress.
4. Social Comparisons: Comparing oneself to peers can foster competition and stress.
5. Time Management: Balancing academics, extracurricular activities, and social life can be overwhelming.

Effects of Stress on Education

1. Decreased Motivation: Stress can lead to disengagement and lack of interest in learning.
2. Impaired Cognitive Function: Stress can affect memory, concentration, and problem-solving skills.
3. Emotional Distress: Stress can lead to anxiety, depression, and mood swings.
4. Physical Health Consequences: Stress can cause headaches, fatigue, and sleep disturbances.
5. Reduced Academic Performance: Chronic stress can negatively impact grades and academic achievement.

Strategies to Manage Stress in Education

1. Time Management: Prioritize tasks, set realistic goals, and take regular breaks.
2. Seek Support: Talk to teachers, counselors, or parents about stress and concerns.
3. Relaxation Techniques: Practice mindfulness, meditation, or deep breathing exercises.

4. Physical Activity: Engage in regular exercise to reduce stress and improve mood.
5. Reframe Thinking: Focus on learning, not just grades, and celebrate small achievements.

Educational Institutions' Role

1. Promote Stress-Reducing Initiatives*: Offer mindfulness programs, counseling services, and stress-management workshops.
2. Foster Supportive Environment: Encourage open communication, empathy, and understanding.
3. Flexible Assessment Methods: Consider alternative assessment methods to reduce standardized testing stress.
4. Teacher Training: Educate teachers on stress recognition and support strategies.
5. Student-Centered Approach: Prioritize student well-being and academic success.

Accordingly to a research, secondary/high school (defined here as junior/lower secondary education and senior/upper secondary education)] (UNESCO, Citation2012) and tertiary (defined here as post-secondary education) (UNESCO, Citation2012) it was self-report by students experiencing ongoing stress relating to their education, which we refer to as academic-related stress, such as pressure to achieve high marks and concerns about receiving poor grades. For example, the Organisation for Economic Co-operation and Development (OECD) recently conducted a survey involving 72 countries and consisting of 540,000 student respondents aged 15–16 years. On average across OECD countries, 66% of students reported feeling stressed about poor grades and 59% reported that they often worry that taking a test will be difficult. The OECD further found that 55% of students feel very anxious about school testing, even when they are well prepared. As many 37% of students reported feeling very tense when studying, with girls consistently reporting greater anxiety relating to schoolwork compared to boys (OECD, Citation2017). This data demonstrates that education and academic performance are a significant source of stress to students. The impact of this ongoing academic-related stress to student outcomes and well-being has not been comprehensively explored. Therefore, the current narrative review explores the impact of academic-related stress on students' academic performance, mental health and well-being.

Academic-related stress and mental health

Previous research indicates that self-reported stress is associated with the presentation of anxious states and lower well-being (Carter, Garber, Ciesla, & Cole, Citation2006; Kessler, Citation1997; Robotham & Julian, Citation2006). The recent above-mentioned OECD survey reports that secondary students who self-report higher levels of academic-related stress also report lower well-being, measured using psychological, social, cognitive and physical components (OECD, Citation2015). A systematic review of 13 studies showed that in individuals undertaking higher education, self-reported levels of stress are associated with poorer quality of life and well-being (Ribeiro et al., Citation2017). Ongoing stress also precipitates the development of more serious mental health issues such as anxiety and depression (Kessler, Citation1997; Moylan, Maes, Wray, & Berk, Citation2013). The prevalence of anxiety is as high as 35% in tertiary students (Bayram & Bilgel, Citation2008; Eisenberg, Gollust, Golberstein, &

Hefner, Citation2007; Ozen, Ercan, Irgil, & Sigirli, Citation2010) and the prevalence of depression is 30% (Ibrahim, Kelly, Adams, & Glazebrook, Citation2013). The reciprocal relationship between stress and depression and anxiety is well established (Dantzer, Citation2012; Dantzer, O'Connor, Lawson, & Kelley, Citation2011; Maes, Citation2008). Indeed, major stressful life events are one of the best predictors of the onset of depression (Kendler et al., Citation1995; Kessler, Citation1997). Accordingly, in young people the first onset of depression is often preceded by major life stressors (Lewinsohn, Allen, Seeley, & Gotlib, Citation1999).

Conclusions

Stress and education are intertwined, but by acknowledging the causes and effects of stress, we can work towards creating a more supportive and stress-reducing educational environment. By implementing effective stress-management strategies and promoting student well-being, we can empower students to succeed academically and thrive emotionally.

References

- American Psychological Association (APA). (2020). Stress in America: Coping with Change.
- National Alliance on Mental Illness (NAMI). (2020). Mental Health and Education.
- World Health Organization (WHO). (2019). Mental Health and Education.
- Taylor and Francis

CNS&E

Current Natural Sciences & Engineering

